

Compositional Reservoir-Flow Simulation for Organic-Rich Gas Shale

O. M. Olorode, I. Y. Akkutlu, and Y. Efendiev, Texas A&M University

Summary

A new-generation compositional reservoir-flow-simulation model is presented for gas-bearing organic-rich source rocks, including convective/diffusive mass-balance equations for each hydrocarbon component in the organic (kerogen), inorganic, and fracture continua. The model accounts for the presence of dispersed kerogen with sorbed-gas corrected dynamic porosity. The Maxwell-Stefan theory is used to predict pressure- and composition-dependence of molecular diffusion in the formation. The equations are discretized and solved numerically by use of the control-volume finite-element method (CVFEM).

The simulation is derived from a new multiscale conceptual flow model. We consider that kerogen is dispersed at a fine scale in the inorganic matrix and that it will be the discontinuous component of total porosity at the reservoir-simulation scale, which could be up to six orders of magnitude larger. A simple mass-balance equation is introduced to enable kerogen to transfer gas to the inorganic matrix that is collocated in the same gridblock. The convective/diffusive transport takes place between neighboring gridblocks only in the inorganic matrix.

The simulation results show that the multiscale nature of the rock is important and should not be ignored because this could result in an overestimation of the contribution of the discontinuous kerogen. We also observe that although adsorbed fluid could contribute significantly to storage in the shale formation, its contribution to production could be severely limited by the lack of kerogen continuity at the reservoir scale and by a low degree of coupling between the organic and inorganic pores. The contribution of the Maxwell-Stefan diffusion to the overall transport in the shale formation increases as the inorganic matrix permeability is reduced because of pressure decline during production.

Introduction

Oil and gas production from organic-rich source rocks is characterized by a sharp decline. This decline is a manifestation of flow-regime transition from an early time, when the production is mainly caused by flow in fractures, to a later period, when the matrix begins to contribute to the production. The extent of the early transient, which could be ephemeral, depends on the presence of fractures and on the physical qualities (conductivity, spatial distribution) of the fracture network. The later period, on the other hand, could take large production times and is characterized by a long tail in production-history plots. Its extent is controlled by the formation qualities. The latter observation and the desire to manipulate decline rates in shale-gas wells for optimal production have resulted in research interest on the shale matrix, in particular its storage and transport mechanisms. In this paper, the terms “resource shale” and “organic-rich shale” are used to refer to organic-rich source rocks, which could include significant volumes of mudstone, silt stone, and carbonate.

Recent investigations on petrophysical characterization of resource shales by use of scanning-electron-microscope (SEM) images and transmission-electron-microscopy images have visually revealed the presence of multiple continua in the shale formation, consisting of the organic matrix also known as kerogen, the inorganic matrix (mainly consisting of clays, quartz, carbonate, pyrite, and feldspars), and the fractures (Loucks et al. 2009, 2012; Ambrose et al. 2012). Kerogen appears in 2D images (Fig. 1) as the finely dispersed phase within the inorganic matrix at the submicron scale, or in 3D images (Fig. 2) as the continuous phase creating its own interconnected network intertwined with the inorganic matrix. Ambrose et al. (2012) gave the first examples of these 3D images at the micron scale, by use of Barnett shale samples as shown in Fig. 2. Akkutlu and Fathi (2012) presented the first set of governing equations honoring these petrophysical observations to describe single-phase flow of gas in shale formation including this duality and coupling of the organic and inorganic matrices. These equations included the contribution of molecular diffusion and surface diffusion in the shale formation. This was necessary, they argued, because the permeability of the shale matrix could be so low that other transport mechanisms could significantly contribute to the overall transport. Recent publications (Sun et al. 2015; Zhang et al. 2015; Akkutlu et al. 2016) on the numerical modeling of transport in shale-gas reservoirs now typically include surface diffusion and Knudsen diffusion in the kerogen-pore network, in addition to molecular diffusion and convection in the kerogen/inorganic-pore network. However, these publications typically ignore the dispersed nature of kerogen, as well as the dependence of the molecular-diffusion coefficients on pressure and composition.

This work is motivated by the general consensus that molecular diffusion in the organic and inorganic matrices can contribute appreciably toward the production performance, and therefore, targets its detailed description in a petrophysical setting that is representative of organic-rich shales. Multicomponent molecular-diffusion theory, hereto referred to as the Maxwell-Stefan diffusion, states that diffusion is a function of pressure, temperature, and composition (Taylor and Krishna 1993). Because it is common to assume that the shale-gas-production process is isothermal, one can ignore the temperature dependence of diffusion. However, pressure is known to drop dramatically near the fracture faces (and more gently farther into the matrix), whereas the hydrocarbon-fluid composition tends to evolve during production (Freeman et al. 2012). These changes in pressure and composition then imply that the diffusion coefficients are not constant.

Yi et al. (2008) introduced the Maxwell-Stefan diffusion to model transport of a binary gas mixture [methane (CH_4) and carbon dioxide] in coals. Their interest was to investigate codiffusion and counterdiffusion phenomena of the mixture components in the presence of adsorption with application into enhanced coalbed- CH_4 recovery. Hoteit and Firoozabadi (2009) and Hoteit (2011) discussed the proper modeling of the diffusion of multicomponent fluids by use of the full tensor of the Maxwell-Stefan diffusion coefficient instead of just a single diffusion coefficient for each hydrocarbon component. They indicated that this could be important in tight reservoirs, where the matrix-permeability values are much lower than in conventional reservoirs. Fathi and Akkutlu (2014) applied the binary Maxwell-Stefan diffusion model to simulate cyclic carbon dioxide stimulation in depleted shale-gas wells. However, we have not

found any other published work showing the use of the Maxwell-Stefan diffusion theory to model the diffusive transport in organic-rich source rocks with more than two hydrocarbon components. This work presents a multicomponent, multicontinuum shale-gas model that captures the pressure dependence and composition dependence of the molecular-diffusion coefficient by use of the Maxwell-Stefan diffusion model. According to this model, the diffusive transport introduces new and intricate nonlinearities into our shale-gas-simulation problem, where the diffusion coefficient of each species needs to be computed in each representative elementary volume (or gridblock in the numerical model) by use of the pressure and composition in the volume at the current timestep.

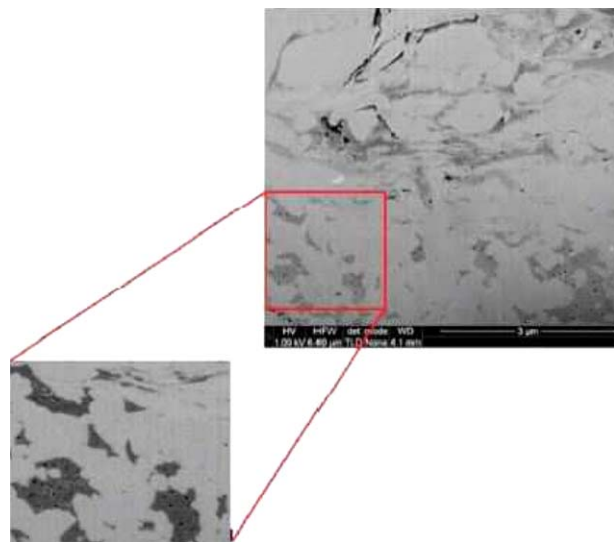


Fig. 1—2D focused-ion-beam/SEM images of an organic-rich shale sample showing finely dispersed kerogen embedded in an inorganic matrix. In these images, black depicts pores, dark gray is kerogen matrix, and light gray is inorganic shale matrix. Images are reproduced from Ambrose et al. (2012).

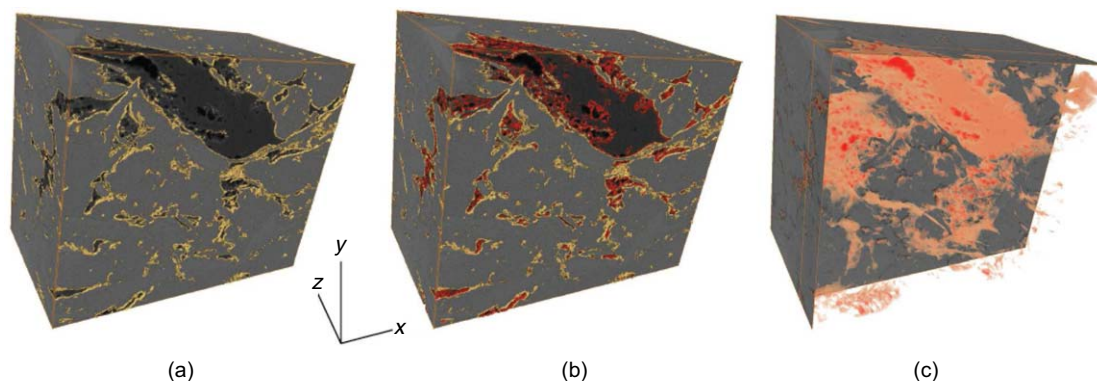


Fig. 2—3D focused-ion-beam/SEM image of an organic-rich shale culled from Ambrose et al. (2012). Sample size is 4 μm high, 5 μm wide, and 2.5 μm deep. (a) The kerogen network is shown with yellow outlines. (b) Yellow also outlines the 3D kerogen network, whereas red outlines the pore spaces. (c) An overlay of porosity and the 3D kerogen network is shown, where the dark orange shows the detected pore spaces within the kerogen.

In addition, we revisit and modify the Akkutlu and Fathi (2012) multicontinuum formulation to capture the discontinuous nature of kerogen. We note that even though the kerogen may create its own continuous phase in the inorganic matrix, the connectivity of the kerogen at a larger scale could be still poor. In addition, molecular transport in the interconnected part of the kerogen-pore network is a relatively slow process compared with flow of gas in the inorganic matrix. Consequently, it is reasonable to assume that kerogen is discontinuous at the reservoir scale. The next section provides a more-detailed argument for a discontinuous kerogen network at the scale of a typical reservoir-simulation gridblock.

A Multicontinuum Model for Multicomponent Single-Phase Transport in Resource Shales

In this work, we present a model that strives to honor the major storage and transport mechanisms that could be expected in resource shales. By use of observations from SEM images (such as in Fig. 1), we propose a model that captures the observation that kerogen is typically discontinuous and dispersed in the inorganic matrix at these micron scales. By use of gas-permeation experiments and history matching, Kang et al. (2011) showed that a large portion of injected gas reaches the organic pores through the inorganic pores. They noted that this is consistent with SEM images that do not show the connectivity of kerogen on scales larger than tens of microns, and they concluded that the coupling between the inorganic and organic matrices is in series. Given that the representative elementary volume or reservoir-simulation gridblock could easily be up to five orders of magnitude larger than SEM images, this work conjectures that these micron-scale “pockets” of kerogen will be discontinuous across simulation gridblocks. We propose a model with an in-series

coupling between the organic and inorganic matrices. **Fig. 3** gives a sketch of the proposed model in one and two dimensions. Fig. 3 shows that the kerogen in each gridblock is not in direct hydraulic communication with the kerogen in the neighboring gridblocks. The sketch of the model clearly shows that the communication between the organic and inorganic pores is in series. The organic pores release reservoir fluids into the inorganic pores, which in turn release their fluids into the hydraulic and/or natural fractures in the reservoir. This work models the hydraulic fractures (and discrete-fracture networks, if present) with the discrete-fracture model, which is discussed in a later section.

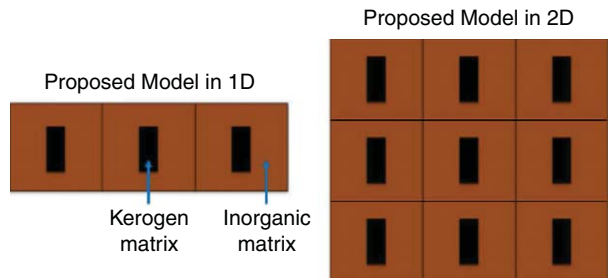


Fig. 3—The proposed model captures the dispersed nature of kerogen in the inorganic matrix.

Mathematical Model for Multicomponent Single-Phase Gas Transport in Shale

The origin of the multicomponent mass-balance equations used in this work could be traced to Akkutlu and Fathi (2012). Some of the specific modifications made in this work are as follows:

- This work models the organic matrix as a dispersed and discontinuous continuum, as inferred from SEM images.
- This work extends the original formulation to a multicomponent system, and uses the Maxwell-Stefan diffusion coefficient to capture the pressure dependence of diffusion.
- This work implements a modified form of the petrophysical model proposed by Ambrose et al. (2012) and Hartman et al. (2012). The modification made in this paper is to correct only the organic pore volume (PV), and not the total PV, by the volume occupied by the adsorbed-gas molecules because we do not expect significant adsorption in the inorganic pores.

Mass-Balance Equations for Gas Components in Inorganic Pores. The equation for the mass balance of the gas component in the inorganic pores is given as

$$-\nabla \cdot J_i^I + \nabla \cdot \left(y_i c_G \frac{k_m}{\mu_g} \nabla p_G \right) + W_{OI}^i = \frac{\partial}{\partial t} [(1 - \epsilon_{kp}) \phi y_i c_G], \dots \dots \dots (1)$$

where

$$J_i^I = -(1 - \epsilon_{kp}) \frac{\phi}{\tau} D_G^i \nabla (c_G y^i), \dots \dots \dots (2)$$

and

$$W_{OI}^i = I_m^T \frac{\epsilon_{kf} \phi}{\tau} D_{kG}^i (y_{k,i} c_{k,G} - y_i c_G) + (1 - \phi) I_m^T D_s^i c_\mu^i + y_{k,i} \frac{I_m^T c_G^O k_m^O}{\mu_g^O} (p_G^O - p_G). \dots \dots \dots (3)$$

The three terms on the right-hand side of Eq. 3 refer to the transfer of reservoir fluids from the organic to the inorganic matrix by molecular diffusion in the pores, surface diffusion, and advection, respectively. The second term in Eq. 3 has been written in terms of the adsorbed concentration in units of g mol per reservoir m³ of rock.

The adsorbed-gas concentration of component *i* can be obtained by use of the extended Langmuir isotherm as follows:

$$c_\mu^i = \frac{c_{\mu s}^i y_{k,i} P_{k,G} / P_L^i}{1 + \sum_{j=1}^{n_c} (y_{k,i} P_{k,G} / P_L^i)} \dots \dots \dots (4)$$

If the maximum adsorbed-gas amount is specified in scf/ton, we can convert this value into the corresponding maximum adsorbed concentration in mol/r-m³ by use of

$$c_{\mu_s} = G_{sL} \rho_{ma} \left(\frac{n}{V} \right)_{sc} \left(\frac{1 \text{ ton}}{907, 185 \text{ g}} \right) \left(\frac{1 \text{ std m}^3}{3.28084^3 \text{ scf}} \right). \dots \dots \dots (5)$$

We note that the term $\epsilon_{kf} \phi$ in Eq. 3 represents the ratio of the organic free-gas PV to the bulk volume. This concept is derived from the petrophysical model presented by Ambrose et al. (2012), where the authors presented a model to account for the PV occupied by gas molecules adsorbed on the organic-pore walls. Their model corrected the effective porosity (ratio of the total PV of connected pores to the bulk volume) in shale by subtracting the adsorbed porosity (ratio of the volume occupied by the adsorbed gas to the bulk volume) from the effective porosity. This work extends their petrophysical model to implement the adsorbed-gas-porosity correction only in the

organic pores. This is because we expect that virtually all the adsorbed gases will be in the organic nanopores. We therefore keep the PV for free gases in the inorganic pores unchanged, but modify the PV available for free gas in kerogen, to account for the space taken up by the adsorbed gas. The free organic porosity (that is, organic PV available for free gas divided by bulk volume) $\varepsilon_{kf}\phi$ can be obtained by first computing the adsorbed porosity ϕ_a by use of Eq. A-4 from Ambrose et al. (2012), which is given as

$$\phi_a = 1.318 \times 10^{-6} M \frac{\rho_b}{\rho_s} \left(G_{sL} \frac{P}{P + P_L} \right) \dots \dots \dots (6)$$

We can write the total organic porosity ϕ_{ekp} as the sum of the adsorbed porosity ϕ_{eka} and the free organic porosity ϕ_{ekf} :

$$\phi_{ekp} = \phi_{eka} + \phi_{ekf} \dots \dots \dots (7)$$

This implies that $\varepsilon_{kp} = \varepsilon_{ka} + \varepsilon_{kf}$, where ε_{kp} is the ratio of the total kerogen PV to the total PV, ε_{ka} is the ratio of the adsorbed PV to the total PV, and ε_{kf} is the ratio of the free kerogen PV to the total PV. Therefore, to obtain ε_{kf} , we compute ϕ_a with Eq. 6, divide ϕ_a by ϕ to obtain ε_{ka} , then subtract ε_{ka} from ε_{kp} to obtain ε_{kf} .

In Eq. 2, we can substitute the definition for effective diffusivity as a function of porosity and tortuosity. This widely used definition for effective diffusivity comes from the Bruggeman equation (Bruggeman 1935):

$$D_{\text{eff}} = \frac{\phi}{\tau} D_G^i \dots \dots \dots (8)$$

where ϕ is the total porosity, and D_G^i is the Maxwell-Stefan diffusion coefficient that will be discussed in the next section. Tortuosity, τ , is defined as the ratio of the actual length of the flow path in the inorganic matrix to the thickness of the porous medium in the flow direction. Similarly, k_m in Eq. 1 is the inorganic-matrix permeability, including the effects of the matrix porosity and tortuosity.

Hu et al. (2015) reported overall tortuosity values ranging from 2 to 12 for some Barnett shale samples by use of the mercury-injection capillary pressure method. However, by use of experimental and analytical methods, respectively, Hu and Ewing (2014) and Revil et al. (2013) showed that this value could be as high as 100. These relatively high values of tortuosity could be a result of the poor pore connectivity expected in these organic-rich source rocks.

Although Eqs. 2 and 3 are written with subscript i , the products of the diffusion coefficients and the mole fractions are evaluated by taking the matrix-vector product of the Maxwell-Stefan diffusion-coefficient matrix and the vector of the mole fractions. This is also how we compute the products of the diffusion coefficients and the mole-fraction gradients.

The mass-balance equation for the total mass of the hydrocarbons in the inorganic matrix is given as

$$-\sum_{i=1}^{n_c} \nabla \cdot J_i^i + \nabla \cdot \left(c_G \frac{k_m}{\mu_g} \nabla p_G \right) + \sum_{i=1}^{n_c} W_{OI}^i = \frac{\partial}{\partial t} [(1 - \varepsilon_{kp}) \phi c_G] \dots \dots \dots (9)$$

The first term on the left-hand side of Eq. 9 represents the molecular diffusion of all the hydrocarbon components. To obtain this value, we simply sum the molecular diffusion of each of the hydrocarbon components given in Eq. 2. Because the Maxwell-Stefan diffusion coefficients are computed for n_c-1 components and relative to the diffusion of the heaviest component, the diffusion of the heaviest component relative to itself is zero, and the sum of the diffusion of all the components defined in this manner is not zero (Taylor and Krishna 1993). The physical interpretation of this is that the hydrocarbon components are able to diffuse toward a fractured well in an ultralow-permeability reservoir, and the sum of the molecular-diffusion fluxes of each component in each gridblock is not zero in this case. The section on Maxwell-Stefan diffusion provides more details on the computation of the coefficients.

Given that the Maxwell-Stefan diffusion-coefficient matrix has a dimension of $(n_c-1) \times (n_c-1)$, Eq. 1 is for the first n_c-1 components of the gas. To obtain the last equation to complete the model, we wrote Eq. 9 instead of the equation for the last hydrocarbon component, n_c . Cao (2002) provides more details on this numerical-modeling approach, but it is worth mentioning that we now have n_c inorganic mass-balance equations in terms of n_c unknowns, $p_G, y_1, y_2, \dots, y_{n_c-1}$.

In this work, gas viscosity μ_g is computed by use of the Lee et al. (1966) correlation, whereas the gas-compressibility factor, Z , is computed by use of the Peng-Robinson equation of state (Peng and Robinson 1976). This Z -factor is then substituted into the real-gas equation to obtain the gas molar density c_G .

Mass-Balance Equations for Gas Components in Organic Pores. The equation for the mass balance of gas component i in the organic pores is given as

$$-W_{OI}^i = \frac{\partial}{\partial t} [\varepsilon_{kf} \phi y_{k,i} c_{k,G} + (1 - \phi) c_{\mu}^i] \dots \dots \dots (10)$$

We note that the diffusive- and advective-transport mechanisms (that were modeled in the inorganic mass-balance equations) are neglected in the organic matrix. This is dependent on the in-series model that assumes that the organic matter (or kerogen) in shales are not expected to be continuous over the typical sizes of reservoir-simulation gridblocks, as explained in the section on the proposed multi-continuum model.

The mass-balance equation for the total mass of hydrocarbons in the organic pores could be written as

$$-\sum_{i=1}^{n_c} W_{OI}^i = \frac{\partial}{\partial t} \left[\varepsilon_{kf} \phi c_{k,G} + (1 - \phi) \sum_{i=1}^{n_c} c_{\mu}^i \right] \dots \dots \dots (11)$$

The organic mass-balance equations add another n_c equations and n_c unknowns, so the total number of equations and unknowns is $2n_c$. The unknowns or primary variables are $p_G, y_1, y_2, \dots, y_{n_c-1}, p_G^O, y_{k,1}, y_{k,2}, \dots, y_{k,n_c-1}$.

Estimation of Shape Factor. Given that the dispersed-kerogen model presented in this work allows the organic matrix to contribute to transport only through its coupling with the inorganic matrix, it is important to accurately estimate the parameters in this coupling term. This section focuses on the estimation of the transient shape factor l_m^i .

Kazemi et al. (1992) presented an equation for estimating the shape factor for any geometry in a dual-porosity model. The shape factor, as shown in Eq. 12, is estimated by use of the volume of the matrix block, the surface open to flow in all directions, and the distances between these surfaces and the center of the matrix block:

$$\sigma_{PSS} = \frac{1}{V} \sum_{i=1}^n \frac{A_i}{d_i}, \quad \dots \dots \dots (12)$$

where σ_{PSS} is the pseudosteady-state shape factor, V is the volume of the matrix block, A_i is the area of each surface, i is the matrix block, d_i is the distance between the center of the matrix block and each surface i , and n is the total number of surfaces of the matrix block. Heinemann and Mittermeir (2012) rederived Eq. 12 and concluded that the equation is exact at pseudosteady-state flow conditions in dual-porosity systems.

In this work, instead of the matrix and fracture continua, we model the organic and inorganic continua. This implies that V , A_i , and d_i in Eq. 12 are for kerogen (instead of the matrix, in a dual-porosity system). The kerogen bulk volume can be easily estimated from ϕ , ε_{kp} , and ε_{ks} , as shown in Appendix A. The corresponding equation for the kerogen pseudosteady-state shape factor l_m^{PSS} is given as

$$l_m^{PSS} = \frac{1}{V^k} \sum_{i=1}^n \frac{A_i^k}{d_i^k}, \quad \dots \dots \dots (13)$$

where the superscript k indicates that these geometric parameters are for the kerogen matrix.

Given the ultralow permeability of shale, coupled with molecular and surface diffusion in the organic matrix, we do not expect to reach a pseudosteady state within the typical productive life of these unconventional resources. However, this implies a need to account for transient flow/transport in shales.

Although any geometry of kerogen can be modeled, we can simplify the model by assuming that the dispersed kerogen has an approximate shape (such as a sphere, cube, cuboid, hexahedra, or tetrahedra). If we assume the approximate geometry of the kerogen is a sphere, and substitute the equations for the volume and total surface area of a sphere into Eq. 13, we obtain

$$l_m^{PSS} = \frac{3}{r_k^2}. \quad \dots \dots \dots (14)$$

Making the radius r_k the subject of the equation for the volume of a sphere, we obtain $r_k = (3V_b^k/4\pi)^{1/3}$. Introducing V_b^k as the kerogen bulk volume and substituting the expression for the radius of a sphere into Eq. 14 yield

$$l_m^{PSS} = \frac{3}{(3V_b^k/4\pi)^{2/3}} \approx 7.8(V_b^k)^{-2/3}. \quad \dots \dots \dots (15)$$

In a similar fashion, we can substitute the equations for the volume, the area, and the distance to the centroid of a cube into Eq. 13. After making the length of a side of the cube the subject of the equation for its volume, we obtain

$$l_m^{PSS} = 12(V_b^k)^{-2/3}. \quad \dots \dots \dots (16)$$

This approach can be extended to different geometries and presented in the following generic form:

$$l_m^{PSS} = \mathcal{G}_A \cdot (V_b^k)^{-2/3}, \quad \dots \dots \dots (17)$$

where \mathcal{G}_A is a geometric factor. Therefore, for a sphere, $\mathcal{G}_A \approx 7.8$, and for a cube, $\mathcal{G}_A = 12$. Appendix B provides examples of the computation of the geometric factor for some geometries. However, given that it is unrealistic to obtain the exact geometry for all the organic matter in a given shale resource, this parameter is recommended to be used as a history-matching parameter, instead of the transient or pseudosteady-state shape factor, as is customarily done in dual-porosity reservoir modeling.

This work recognizes the fact that we do not expect pseudosteady-state flow during the typical productive life of shale-gas reservoirs. Therefore, in the coupling term, we use a model dependent on the Zimmerman transient shape factor (Zimmerman et al. 1993) instead of the Warren-Root pseudosteady-state shape factor (Warren and Root 1963). Azom and Javadpour (2012) applied the Zimmerman transient shape factor in terms of pseudopressures, whereas Lu et al. (2008) applied it in terms of concentration (or molar density). In this work, we write the simplified expression for the transient shape factor, presented by Azom and Javadpour (2012), in terms of concentration as follows:

$$l_m^T = \frac{2c_{ki} - (c_k - c)}{2(c_{k,i} - c_k)} l_m^{PSS}. \quad \dots \dots \dots (18)$$

To clearly show that Eq. 18 approaches the pseudosteady-state shape factor when c_k tends to c , we simplify the equation further by expanding the numerator and separating out the two fractions to obtain

$$l_m^T = \left(0.5 + 0.5 \frac{c_{k,i} - c}{c_{k,i} - c_k} \right) l_m^{PSS}. \quad \dots \dots \dots (19)$$

We define a transient factor \mathcal{T}_f to be equal to the bracketed term on the right-hand side:

$$\mathcal{T}_f = \left(0.5 + 0.5 \frac{c_{k,i} - c}{c_{k,i} - c_k} \right). \quad \dots \dots \dots (20)$$

Substituting this as well as Eq. 17 into Eq. 19 yield:

$$l_m^T = \mathcal{G}_A \mathcal{T}_f (V_b^k)^{-2/3}. \quad \dots \dots \dots (21)$$

As demonstrated by Zimmerman et al. (1993), the transient coupling term captures the correct scaling of the matrix pressure (in this case, organic-gas concentration) with the square root of time ($t^{1/2}$), whereas the corresponding pseudosteady-state coupling term scales incorrectly with time (t). For this reason, the use of the shape factor as a constant history-matching parameter could be erroneous. We also note that the pseudosteady-state shape factor (and consequently the transient shape factor) for each gridblock, as shown in Eq. 13, is a function of its corresponding volume. Therefore, the use of a constant shape factor in all the gridblocks of a numerical model with varying gridblock sizes could lead to significant errors in the coupling term. This error could be further magnified in models with grid refinements, where the smallest cells could be orders of magnitude smaller than the largest ones.

It is important to note that the remarks on shape factors in this section are also applicable in conventional dual-porosity systems.

Maxwell-Stefan Diffusion. Most of the published works on molecular diffusion in porous media assume a constant effective diffusion coefficient for each of the hydrocarbon components (Sun et al. 2015; Wasaki and Akkutlu 2015; Xiong et al. 2015). In this work, we note that the kinetic theory of gases indicates that the diffusion coefficient is inversely proportional to pressure. This implies that the diffusion coefficients for an Eagle Ford shale-gas reservoir with a pressure of approximately 11,400 psi (Orangi et al. 2011) could be as little as approximately 35% of that for a Barnett shale-gas reservoir with a pressure of approximately 4,000 psi (provided that the temperatures and mole fractions of the hydrocarbon components are not too different). The use of the Maxwell-Stefan diffusion coefficient provides a means to estimate the diffusion coefficient for any reservoir, given its pressure and gas composition. It also allows us to effectively capture the dependence of diffusion on pressure and composition. Taylor and Krishna (1993) noted that the Maxwell-Stefan diffusion is capable of modeling osmotic diffusion, reverse diffusion, and diffusion at a diffusion barrier, whereas the Fickian diffusion as well as the effective diffusion model could be limited in these cases. This work uses the generalized Maxwell-Stefan diffusion equation to estimate the diffusion coefficient for the hydrocarbon components in an open medium. The corrections for a tortuous porous medium were explained previously.

Details on the theory and some applications can be found in Taylor and Krishna (1993). In Eq. 22, we simply give the final form of the Maxwell-Stefan diffusion equation:

$$J = -c \mathcal{B}^{-1} \Gamma \nabla \mathbf{y}. \quad (22)$$

Comparing Eq. 22 with Fick's law for diffusion, we can obtain a Fickian-type matrix of coefficients for the Maxwell-Stefan equation. That is,

$$D = \mathcal{B}^{-1} \Gamma. \quad (23)$$

The equations to obtain the drag matrix \mathcal{B} are given by Taylor and Krishna (1993):

$$\begin{aligned} \mathcal{B}_{ii} &= \frac{y_i}{D_{in}} + \sum_{k=1; i \neq k}^n \frac{y_k}{D_{ik}}, \\ \mathcal{B}_{ij} &= -y_i \left(\frac{1}{D_{ij}} - \frac{1}{D_{in}} \right), \end{aligned} \quad (24)$$

where D_{ij} , D_{in} , and D_{ik} are the Maxwell-Stefan diffusion coefficient for any pair of components, and can be obtained from the kinetic theory of gases. In this work, we use the Fuller et al. (1966) correlation, which is dependent on the kinetic theory of gases. The parameters for this correlation are readily available in Fuller et al. (1969), and this correlation is recommended by Danner and Daubert (1983) and by Reid et al. (1987).

The equation for the thermodynamic factor is given by Walas (1985):

$$\Gamma = \delta_{ij} + y_i \left. \frac{\partial \ln \Phi_i}{\partial y_j} \right|_{T,P,\Sigma}, \quad (25)$$

where Φ in this equation represents the fugacity coefficient and the subscript Σ indicates that the differentiation of $\ln \Phi_i$ with respect to mole fraction y_j should be performed such that the mole fractions of all other components are kept constant, except the n th. The fugacity coefficient is computed by use of the Peng-Robinson equation of state (Peng and Robinson 1976).

It is important to note that the equations for \mathcal{B} given previously assume that the sum of the molecular-diffusion fluxes of each component is equal to zero. If instead we define the molecular diffusion relative to the heaviest component in the mixture, n_c , the molecular-diffusion flux of that component will be zero, whereas the sum of all the other $n_c - 1$ components will be nonzero. To obtain the corresponding \mathcal{B} in this case, we use the modified equation from Taylor and Krishna (1993):

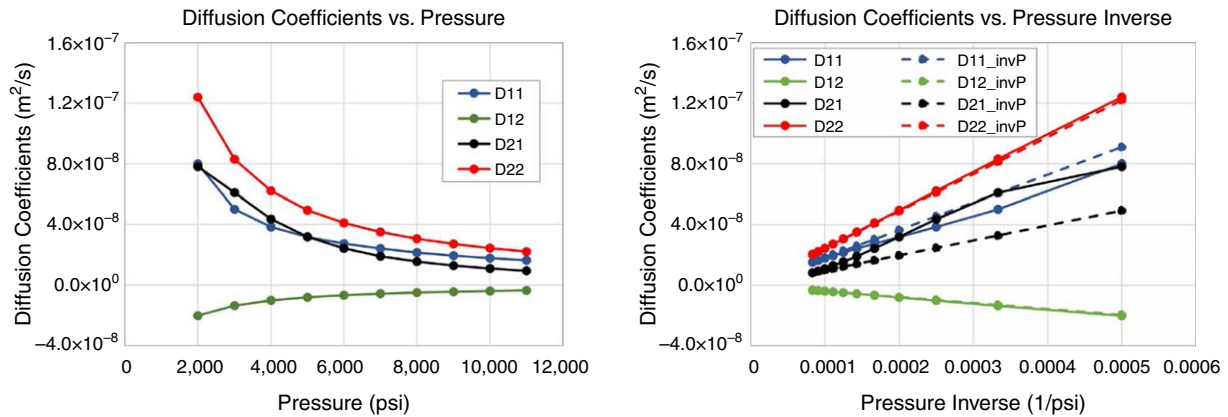
$$\begin{aligned} \mathcal{B}_{ii}^{n_c} &= \sum_{k=1; i \neq k}^n \frac{y_k}{D_{ik}}, \\ \mathcal{B}_{ij}^{n_c} &= -\frac{y_i}{D_{ij}}. \end{aligned} \quad (26)$$

The equations presented for the computation of the Maxwell-Stefan diffusion coefficient were programmed and validated against several examples given in Taylor and Krishna (1993). By use of the mole fractions specified in **Table 1**, we computed the 2×2 matrix of diffusion coefficients (for a three-component system) at different pressures, ranging from 12,000 to 2,000 psi. Each element of this matrix of diffusion coefficients is then plotted against pressure in **Fig. 4a**. The plot shows that the diffusion coefficients increase as the pressure drops.

To confirm whether the matrix of diffusion coefficients is strictly inversely proportional to pressure, we plot these diffusion coefficients against the inverse of pressure. The dotted lines shown in **Fig. 4b** show rough estimates of the diffusion coefficients assuming a strictly inverse proportionality with respect to pressure, whereas the solid lines are the results obtained with the code developed by use of the rigorous procedure described in this section. **Fig. 4** shows that this rough approximation could be acceptable given the considerable computational efficiency of this approximation in comparison with the rigorous computation of the diffusion coefficients at each Newton iteration and simulation timestep. It is worth noting that although the kinetic theory of gases and the Fuller et al. (1966) correlation show that the binary-diffusion coefficients are strictly inversely proportional to pressure, the deviation of the matrix of diffusion

Parameters	SI Unit	Field Unit
Fracture half-length, x_f	450 m	1,476 ft
Fracture width, w_f	3 mm	0.00984 ft
Reservoir thickness, h	100 m	330 ft
Matrix permeability, k_m	$1.0 \times 10^{-19} \text{ m}^2$	$1.0 \times 10^{-4} \text{ md}$
Fracture permeability, k_f	$5.0 \times 10^{-11} \text{ m}^2$	$5.0 \times 10^4 \text{ md}$
Matrix porosity, ϕ	0.04	0.04
Fracture porosity, ϕ_{frac}	0.33	0.33
Temperature, T	50°C	122°F
Well radius, r_w	0.1 m	0.32 ft
Initial reservoir pressure, p_i	$2.76 \times 10^7 \text{ Pa}$	4,000 psia
Initial mole fractions, z_i	[0.85, 0.1, 0.05]	[0.85, 0.1, 0.05]
Flowing bottomhole pressure (BHP), p_{wf}	$1.03 \times 10^7 \text{ Pa}$	1,500 psia
Total organic carbon	5%	5%
Ratio of kerogen PV to matrix PV, ϵ_{kp}	0.35	0.35
Tortuosity, τ	2–10	2–10
Biot constant, α	0.5	0.5
Confining pressure, P_c	$1 \times 10^8 \text{ Pa}$	15,000 psi
Effective stress, P_1	$1.8 \times 10^8 \text{ Pa}$	26,000 psi
G_{sL} of C_1 , C_2 and C_3	[184.5, 299.7, 589.6] g mol/r-m ³	[56, 91, 179] scf/ton
Langmuir pressure, p_L , for C_1 , C_2 , C_3	[10.8, 5.6, 5.8] $\times 10^6 \text{ Pa}$	[1,562, 811, 844] psi
Sorbed gas density, ρ_s , for C_1 , C_2 , C_3	[371, 460, 486] kg/m ³	[23.2, 28.7, 30.3] lbm/ft ³
Bulk density, ρ_b	2,500 kg/m ³	$1.56 \times 10^5 \text{ lbm/ft}^3$

Table 1—Reservoir parameters and their basis values used in the simulations.



(a) The diffusion coefficient shows a nonlinear relationship with pressure. It increases as the reservoir pressure drops in response to production.

(b) The relatively close proximity of the dotted lines to the solid lines suggests that we could assume that the diffusion coefficient is roughly inversely proportional to pressure.

Fig. 4—The diffusion-coefficient plots show a strong dependence of the diffusion coefficient on pressure. (a) The diffusion coefficient shows a nonlinear relationship with pressure. It increases as the reservoir pressure drops in response to production. (b) The relatively close proximity of the dotted lines to the solid lines suggests that we could assume that the diffusion coefficient is roughly inversely proportional to pressure.

coefficients from this strict proportionality comes from the nonlinear dependence of the thermodynamic factor Γ on pressure. We recall that the matrix of diffusion coefficients is a matrix multiplication of the inverse of the drag matrix \mathcal{B} and the thermodynamic factor Γ . In Fig. 4b, we observe that the red and green lines are almost identical to the perfect inverse-pressure relationship, whereas the blue and black lines (corresponding to diffusion coefficients D11 and D21) show some differences. These differences are caused by the nonlinear dependence of Γ on pressure, as implied by Eq. 25. We may not be able to interpret each element of the diffusion-coefficient matrix as corresponding to a single component or pair of components because they are actually influenced by all the hydrocarbon components in the reservoir fluid.

The change in the Maxwell-Stefan diffusion coefficients in response to a change in composition (during production) was less than 4% on the diagonal terms. The mole fractions were varied within the range that was observed during the simulation runs, and the diffusion coefficients were computed at 12,000 and 2,000 psi. The greatest change in the matrix of diffusion coefficients (<29%) was on the second row, first column, whereas the other off-diagonal element was less than 9%. Comparing these changes in diffusion coefficient with the changes in response to pressure drop, we could neglect the composition dependence of the Maxwell-Stefan diffusion coefficients in exchange for improved computational efficiency.

Given that permeability is expected to decrease as pressure decreases during production, we can infer that the contribution of molecular diffusion to production in these ultralow-permeability reservoirs could become increasingly more significant, particularly in high-pressure shale reservoirs where we expect a large drop in pressure from the initial reservoir pressure to the wellbore pressure.

CVFEM Discretization of the Mass-Balance Equations

The CVFEM is a numerical discretization scheme that basically combines the advantages of the finite-element method with the advantages of the finite-volume method. It is locally conservative, like the finite-volume methods, and like the finite-element methods, it allows the flexibility of gridding with triangular or quadrilateral elements. Lemonnier (1979), Forsyth (1990), Fung et al. (1992), Chen et al. (2006), and others have demonstrated the use of the CVFEM to model fluid flow in petroleum reservoirs. Voller (2009) detailed the use of this method to model solid deformation and fluid flow. Cordazzo et al. (2003, 2005) and Hurtado et al. (2007) showed that the CVFEM can be improved by simply specifying porosity and permeability to be constant over each finite element (instead of having these properties specified at the nodes). This improved form of the CVFEM was shown to give lower truncation errors and better accuracy in the modeling of heterogeneities (Cordazzo et al. 2003). Eymard and Sonier (1994) showed some mathematical and numerical properties of the CVFEM. They performed some numerical simulations and concluded that the CVFEM has several mathematical and numerical advantages over the conventional control-volume finite-difference method, and no disadvantages were reported.

Eqs. 1 and 10 can be written in a general form:

$$\nabla \cdot F_i^\mu + B_i^\mu = \frac{\partial}{\partial t} M_i^\mu, \dots \dots \dots (27)$$

where μ represents the inorganic and organic matrices ($\mu = I, O$), $B_i^I = W_{OI}$, $B_i^O = -W_{OI}$,

$$F_i^O = 0, \text{ and } F_i^I = J_i^I + y_{iCG} \frac{k_m}{\mu_g} \nabla p_G.$$

We note that the simplification of F_i^O to zero is because we assume that kerogen is typically dispersed or discontinuous at the reservoir scale, as explained in the section on the proposed model.

After performing temporal discretization by use of the implicit Euler scheme, we integrate Eq. 27 over a control volume, Ω , and use the divergence theorem on the integral of the flux term to obtain

$$\int_{\Omega} \nabla \cdot F_i^\mu \cdot d\Omega + \int_{\Omega} B_i^\mu d\Omega = \int_{\Omega} \frac{M_i^{\mu,k+1} - M_i^{\mu,k}}{\Delta t} d\Omega \dots \dots \dots (28)$$

The integration of the second term on the left-hand side as well as the right-hand terms of Eq. 28 can be performed by use of nodal lumping. For the control volume centered at m in Fig. 5, we can evaluate the surface integral as follows:

$$\int_{\partial\Omega} F_i^\mu \cdot ndS = \sum_{n=1}^{n_m} \int_{A^n} F_i^\mu \cdot ndA = \sum_{n=1}^{n_m} \int_{A^n, \text{face1}} F_i^\mu \cdot ndA + \int_{A^n, \text{face2}} F_i^\mu \cdot ndA \dots \dots \dots (29)$$

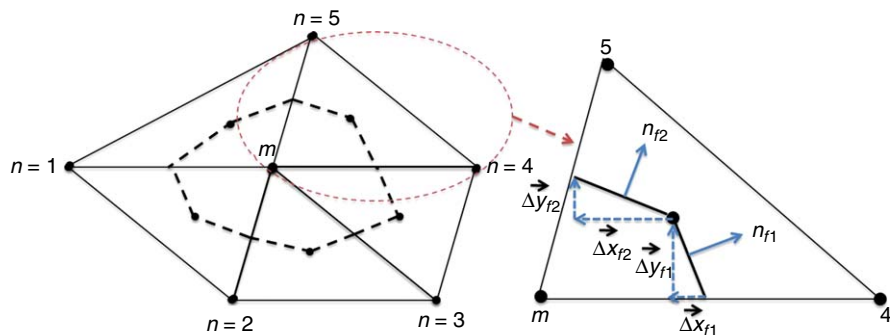


Fig. 5—Control volume centered at m , showing its region of support, $n = 1, \dots, 5$. Subscripts $f1$ and $f2$ refer to Faces 1 and 2 of the control volume (centered at m) within the element $m, 4, 5$, shown on the right.

For more details on the evaluation of the control-volume discretization of the flux terms, the reader is referred to Fung et al. (1992), Chen et al. (2006), and Voller (2009). After following the procedure detailed in Voller (2009) and multiplying both sides of the discretized equation by Δt , we can write the discrete form of the equation as

$$R_i^p = \Delta t \sum_{n=1}^{n_n} (a_m^j \Psi_m + a_n^j \Psi_n + a_{n+1}^j \Psi_{n+1}) + \Delta t B_{i,m}^\mu V_m - M_{i,m}^{\mu,k+1} V_m + M_{i,m}^{\mu,k} V_m \approx 0, \dots \dots \dots (30)$$

where we have written the equation in terms of each of the diffusive processes, with index j , ranging from unity to the number of flux terms n_F in the mass-balance equation. The coefficients of the primary variable (a_m^j , a_n^j , and a_{n+1}^j) represent the linearized coefficient of pressure gradient, which entails the mobility and geometric terms in the case of advective transport, and they refer to the linearized coefficient of the concentration gradient, which entails the effective diffusivity and geometric terms in the case of diffusive transport. Here, for instance, we note that for the gas-phase advection term in the inorganic matrix, $a_m \Psi_m = a^{G,adv} P_{G,m}^I$, where $a^{G,adv}$ is the linearized coefficient of the inorganic-pore pressure of gas in a control volume centered at m . All other flux terms on the left-hand side of the mass-balance equations are defined in a similar fashion.

Writing this equation for the inorganic matrix yields

$$R_i^I = \Delta t \left[\sum_{n=1}^{n_n} (a_m^j \Psi_m + a_n^j \Psi_n + a_{n+1}^j \Psi_{n+1}) \right]^I + \Delta t B_{i,m}^I V_m - M_{i,m}^{I,k+1} V_m + M_{i,m}^{I,k} V_m \approx 0, \dots \dots \dots (31)$$

where all the Ψ_m , Ψ_n , and Ψ_{n+1} terms are evaluated at the p th Newton-Raphson iteration and at the current timestep $k + 1$.
 Going through an identical procedure, we can obtain the residual of the organic mass-balance equation as

$$R_i^O = \Delta t B_{i,m}^O V_m - M_{i,m}^{O,k+1} V_m + M_{i,m}^{O,k} V_m \approx 0. \dots \dots \dots (32)$$

These residuals are differentiated with respect to each of the primary variables to obtain the Jacobian matrix. The resulting linear system of equations is solved for the changes in the primary variables, which are then used to update these primary variables in a Newton iteration. After updating the primary variables in the Newton iteration, we move on to the next timestep and repeat this procedure.

Discrete-Fracture Model

All the equations presented up to this point implicitly assume that the matrix is not fractured. In this section, we focus on how we can model hydraulic and natural fractures in shale-gas reservoirs by use of the discrete-fracture model (DFM). The DFM was originally developed as a better alternative to the dual-continuum models in naturally fractured reservoirs, where the properties of the individual fractures in the fracture network vary, and the fractures may be unevenly distributed across the reservoir domain. In addition, the DFM is computationally efficient because the fractures are modeled at a dimension of $n-1$, where n is the number of dimensions of the reservoir (Noorishad and Mehran 1982). An attempt to explicitly model all the natural fractures in a reservoir could be very tedious, unrealistic, and unnecessary, given the relative accuracy of the DFM in comparison with an explicit model for the fracture. Kim and Deo (2000) presented some examples of this comparison, though in the context of natural fractures. Li and Lee (2008) also used the DFM to model natural fractures in black-oil reservoirs, and discussed an implementation of the DFM for long fractures that intersect wells. In the next section, we show a corresponding comparison of the results from DFM with an explicit-fracture model for hydraulic fractures.

Given the tendency for shale- and tight gas reservoirs to be naturally fractured, the use of the DFM to model these unconventional resources could provide a consistent, efficient, and accurate treatment of hydraulic and natural fractures. Multiscale models derived from the DFM have also been developed to further improve the computational efficiency in the modeling of fractured shale-gas reservoirs (Efendiev et al. 2015; Akkutlu et al. 2016). A simple way of implementing the DFM in a CVFEM simulator involves a linear superposition of the matrix and fracture domains. That is, the total domain could be decomposed into these two subdomains. Programmatically, this means that we add the residual of the mass-balance equations of the hydrocarbon components in the inorganic matrix to the mass-balance equations of the hydrocarbon components in the fracture. Monteagudo and Firoozabadi (2004) detail the application of this approach in a control-volume method.

Fig. 6 shows the discretization of a single vertical fracture in a reservoir modeled by use of the DFM, with all dimensions shown in meters. This grid (as well as all other grids used in the simulation studies presented) was generated by use of Gmsh, a free 3D finite-element grid generator (Geuzaine and Remacle 2009). Fig. 7 provides a sketch illustrating how the hydraulic fractures were modeled with the DFM and CVFEM. This sketch focuses only on the finite elements and control volumes in the region near the hydraulic fracture. The triangles are the finite elements used to discretize the domain, whereas the dotted lines enclose the control volumes that are implicitly or numerically constructed around each node (or vertex) in the domain. In the 2D geometrical domain of the reservoir, the fracture is represented as a line. However, in the computational model, we fully account for the volume of the fractures by use of the length, width, and height of the fracture.

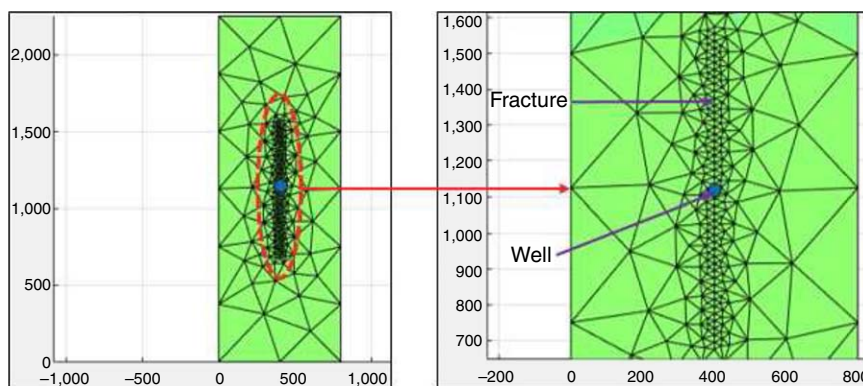


Fig. 6—The unstructured gridding of the reservoir domain with Gmsh is shown. The physical dimension of the reservoir is also shown.

For a 2D reservoir, we can write the residual form of the 1D mass-balance equation for each species in the fracture in the same form as Eq. 30:

$$R_i^f = \Delta t \sum_{f=1}^{n_f} h w_f y_i^f c_G^f \frac{k_f}{\mu_g^f} \left(\frac{p_j^f - p_i^f}{|ij|} \right) - h l_f w_f [(\phi^f c^f)^{k+1} - (\phi^f c^f)^k] \approx 0. \dots \dots \dots (33)$$

The residual equation for the fracture, given in Eq. 33, is simply added to the matrix residual equation, given in Eq. 30, and the equation is solved as detailed previously. It is worth noting that this simple addition of the two equations ensures that the flux across any

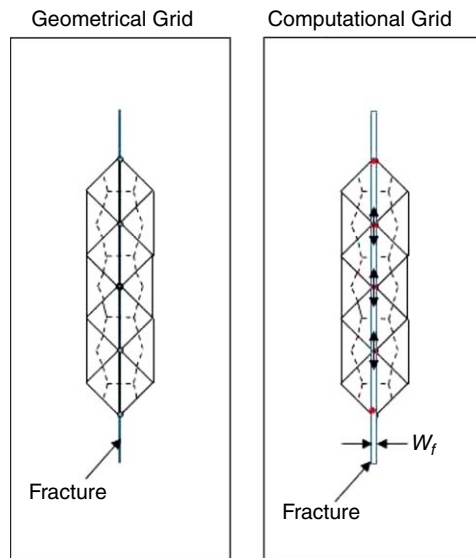


Fig. 7—The fracture is represented as a line in the geometrical domain, but as a 2D plane with an aperture (and corresponding volume) in the computational domain.

pair of fracture nodes is added to the flux on the interface between the two control volumes centered on these two nodes. Therefore, the total flux across the surface of any control volume with a fully penetrating fracture includes the additional flux between the control volume and all neighboring control volumes connected by a fracture. To ensure that the accumulation of reservoir fluid in the fracture is correctly modeled, we subtract the volume of each fracture segment from the volume of the control volume in which the fracture segment is located. This reduced volume is the bulk volume of the matrix, which is used in Eq. 30. Syihab (2009) provides more details on this volume correction, as well as the treatment of the geometrical and computational domains.

Results and Analysis

This section discusses the results obtained from the numerical simulations performed in this work. The physical description of the single vertically fractured shale-gas well modeled is given in Figs. 6 and 7. All the results presented in this section assume that the permeability of the nanoporous organic pores is so small that we do not expect significant advective transport from the organic pores into the inorganic pores, so we neglect the advective term in Eq. 3. Furthermore, to avoid the complexities associated with the multicomponent surface diffusion from the organic pores into the inorganic pores, we neglect the second term in Eq. 3. These two assumptions imply that the simulation results presented are dependent on the coupling of the organic pores to the inorganic pores by molecular diffusion. However, we account for the contribution of the adsorbed fluids to storage in the accumulation terms on the right-hand side of Eq. 10. The degree of coupling between the organic and inorganic pores is therefore controlled by the coefficient of the concentration gradient between these pores. The expression for this “coupling coefficient” (C_c) can be obtained from Eq. 3 as

$$C_c = l_m^T \frac{\varepsilon_{kf} \phi}{\tau} D_{kG}^i \dots \dots \dots (34)$$

Substituting the definition of l_m^T given in Eq. 21, we can write Eq. 34 as

$$C_c = \frac{\varepsilon_{kf} \phi}{\tau} \mathcal{G}_A \mathcal{T}_f (V_b^k)^{-2/3} D_{kG}^i \dots \dots \dots (35)$$

Given the expected uncertainties in tortuosity τ and the kerogen geometric factor \mathcal{G}_A , we can group these two terms together by defining a coupling constant ζ as follows:

$$\zeta = \frac{\mathcal{G}_A}{\tau} \dots \dots \dots (36)$$

This allows us to perform sensitivity studies on ζ , which is basically an unknown constant in the simulation model. Substituting this definition for ζ into Eq. 35 yields

$$C_c = \zeta \varepsilon_{kf} \phi \mathcal{T}_f (V_b^k)^{-2/3} D_{kG}^i \dots \dots \dots (37)$$

For completeness, we note that ε_{kf} and ϕ could be estimated from petrophysical analysis and are considered as inputs (specified in Table 1) in this work. To estimate the kerogen bulk volume, V_b^k , we use Eq. A-8, which is derived in Appendix A. \mathcal{T}_f is estimated by use of Eq. 20, and D_{kG} is estimated from the Maxwell-Stefan diffusion model, as described in the Maxwell-Stefan Diffusion subsection.

Shale-Gas-Model Parameters. Table 1 outlines the reservoir parameters for the model studied in this work. These parameters are derived from the Barnett shale-gas-reservoir properties obtained from Akkutlu and Fathi (2012), Olorode et al. (2013), and Hu et al. (2015). The sorption parameters were obtained from Ambrose (2011), and the physical dimensions of the reservoir system modeled are given in Fig. 6. In all cases simulated, we model the production well as a constant-pressure inner boundary, whereas the external boundaries of the reservoir are modeled as no-flow boundaries.

Model Validation. In this subsection, we discuss the validation of the numerical simulator developed (called TamCVFEM) against Eclipse 300, a commercial compositional reservoir simulator. The model compared corresponds to a tight gas reservoir with a porosity of 4%, a permeability of 100 nd, and without an organic matrix. Additional details on the tight-gas reservoir can be found in Table 1. **Figs. 8a and 8b** show a comparison of TamCVFEM with Eclipse 300 on rate and cumulative plots, respectively. The differences in the production rates at early time (in Fig. 8a) could be attributed to numerical differences between the discretization schemes used in the two simulators. The hydraulic fracture is modeled explicitly in Eclipse 300, whereas the DFM is used in TamCVFEM. These plots show that the developed simulator is capable of modeling a compositional gas reservoir with hydraulic (or discrete) fractures.

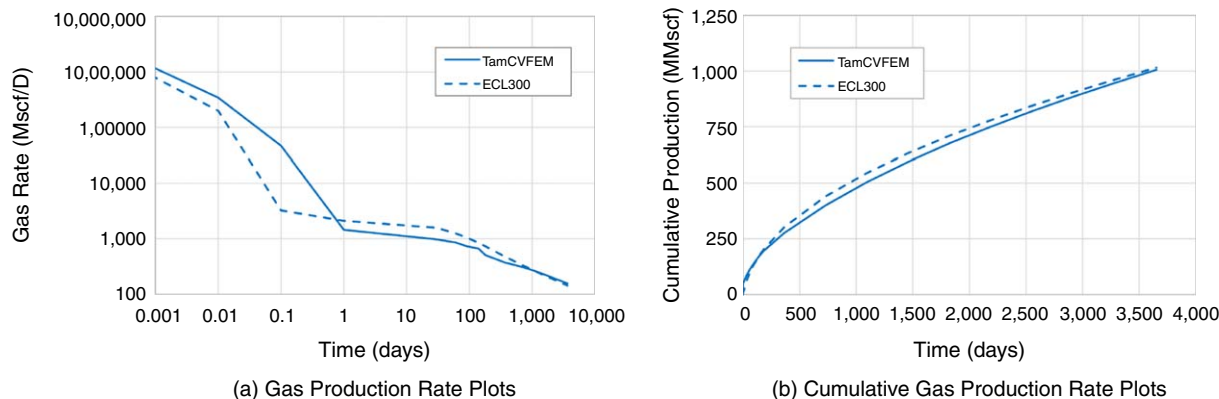


Fig. 8—Comparison of the production plots validates TamCVFEM against Eclipse 300: (a) Gas-production-rate plots. (b) Cumulative-gas-production plots.

Contribution of Molecular Diffusion to Transport in the Inorganic Shale Matrix. In the results shown in **Figs. 9a and 9b**, we model a system that corresponds to the inorganic matrix of a shale-gas reservoir; that is, $\epsilon_{kp} = 0$. The idea is to evaluate the relative contribution of molecular diffusion as a means of transport of fluids in the inorganic matrix of a shale-gas reservoir. The dotted lines in Fig. 9a correspond to the cases where we model advective transport only, whereas the solid lines correspond to the scenarios where we model both molecular diffusion and advection. The logarithmic scale in Fig. 9a tends to amplify the differences between production profiles at very low values, and it compresses or masks the differences at high values of production rate. We observe from both Fig. 9a and Fig. 9b (as well as all other simulations in this work) that the contribution of the diffusive transport in the inorganic pores is negligible at 100 nd, which is the base case that could be representative of a resource shale. We observe increased contribution of diffusive transport at 10 and 1 nd. However, in addition to the production plots with and without diffusion at 100, 10, and 1 nd, we added a case at 100 nd, where the tortuosity was set to 2 (instead of the base-case value of 7), which is the lowest value in the range given in Table 1. The result, as well as all other cases at 100 nd, showed that advective transport dominates diffusive transport in an inorganic matrix with a permeability of 100 nd.

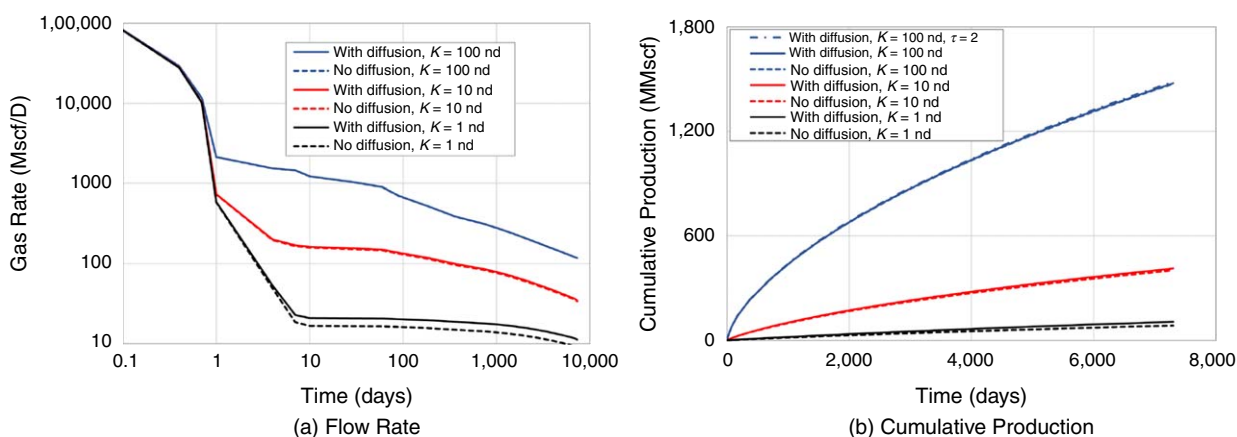


Fig. 9—Effect of diffusion on shale-gas production. The results indicate that diffusion is not important in the inorganic pores at matrix-permeability values of 100 nd or higher. (a) flow rate; (b) cumulative production.

It is important to note that the relatively large cumulative production values of the 100-nd case could mask the magnitude of the contribution of molecular-diffusion contribution at 10 and 1 nd. **Fig. 10** gives the corresponding cumulative production curves without the 100-nd cases. In addition, Fig. 10 shows the increased contribution of molecular diffusion if the tortuosity is set to 2 instead of the base-case value of 7.

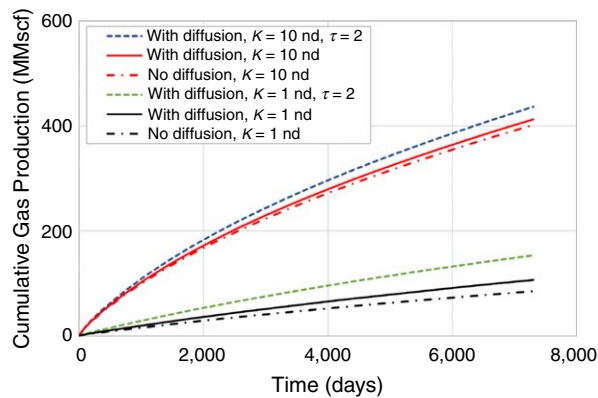


Fig. 10—The contribution of diffusion to production appears increasingly significant at lower matrix-permeability values (10 nd or lower).

At 100 nd, virtually all the simulation cases performed at 100 nd appeared nearly indistinguishable on the log-log rate plots, so all other results presented in this paper show the cumulative gas-production plots only. To clarify, although the results presented in this section show that advective transport dominates molecular diffusion in an inorganic matrix with a permeability of 100 nd, this is not the case in the organic pores where diffusive transport could be the dominant transport mechanism.

Effect of the Coupling Constant ζ on Shale-Gas Production. We defined the coupling constant ζ as the ratio of the geometric factor \mathcal{G}_A to the tortuosity τ in Eq. 36. The section on shape factor, as well as Appendix B, discusses the computation of the geometric factor \mathcal{G}_A . **Fig. 11** shows the production performance of the representative Barnett shale studied at different values of ζ . We observe that the plot shows observable increase in cumulative production at relatively low values of ζ . At ζ -values greater than 27, we do not observe any significant increases in cumulative production. This indicates that beyond a particular level of coupling between the organic and the inorganic matrix, further increases in the magnitude of the coupling do not result in increased production because the organic and inorganic pores could be said to be “fully coupled” at these values of the coupling factor. A possible extension of the interpretation of this result is a hypothesis that further increases in the transport of gases in the nanoporous organic matrix (caused by surface diffusion or additional adsorbed-phase transport) may not lead to any significant increase in gas production if the organic pores are already fully coupled with the inorganic pores.

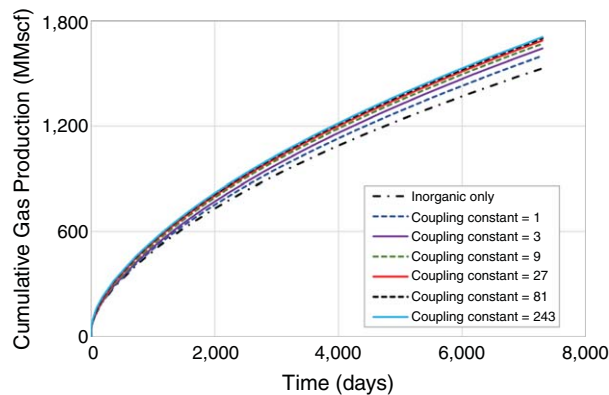


Fig. 11—The sensitivity runs at increasing values of the coupling constant show that the increase in cumulative production at increasing levels of the coupling constant becomes less significant at higher values of the coupling constant.

Fig. 12 shows the corresponding ζ pressure profiles at the different values of ζ . There was no observable difference in the inorganic-pore-pressure profiles, so we show only one inorganic-pore-pressure profile together with the organic-pore-pressure profiles at the corresponding ζ -values. All pressure profiles shown in Fig. 12 include the correction for the PV occupied by the adsorbed-gas molecules. Given the negligible contribution of diffusion to transport at a matrix permeability of 100 nd, the simulated changes in the composition of the produced fluid were negligible.

Importance of the Nonlinearity in the Coupling Coefficient \mathcal{C}_c . In this section, we study the effect of the nonlinearity in the terms comprising the coupling coefficient. The expression for the coupling coefficient is given in Eq. 37. An inspection Eq. 37 shows that the nonlinear terms include the transient factor \mathcal{T}_f and the diffusion coefficient. The results presented in **Fig. 13** indicate that the nonlinearities in the coupling coefficient result in an increase in the estimated production, and this effect is more significant at lower degrees of coupling between the organic and inorganic matrices. This is expected because the transient factor is always greater than unity, and only becomes equal to unity at pseudosteady state. In addition, the inverse pressure dependence of the diffusion coefficient is such that the diffusion coefficient increases as pressure drops during production.

Effect of the Correction for the PV Occupied by Sorbed-Gas Molecules. **Fig. 14** shows the effect of the correction of the free-gas PV to account for the PV taken up by the gas molecules adsorbed on the surfaces of the organic pore walls. The comparison of the case

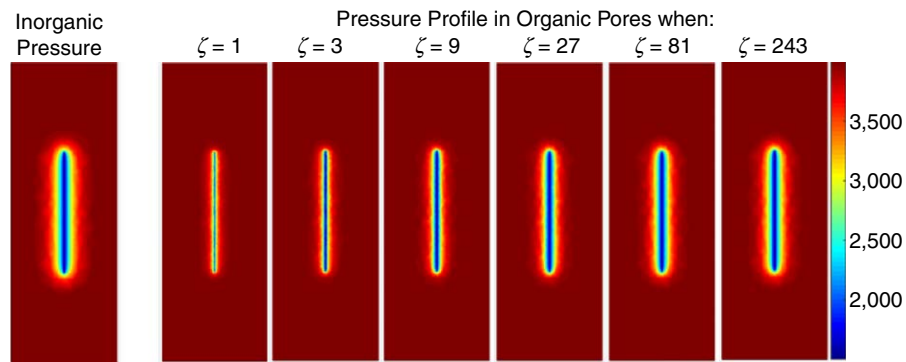


Fig. 12—Organic-pore-pressure profile after 20 years of production shows that the organic matrix is depleted more at higher values of the coupling constant ζ . We only show one inorganic-matrix-pressure profile because there is no observable difference in the inorganic-pore-pressure profile at the different values of ζ .

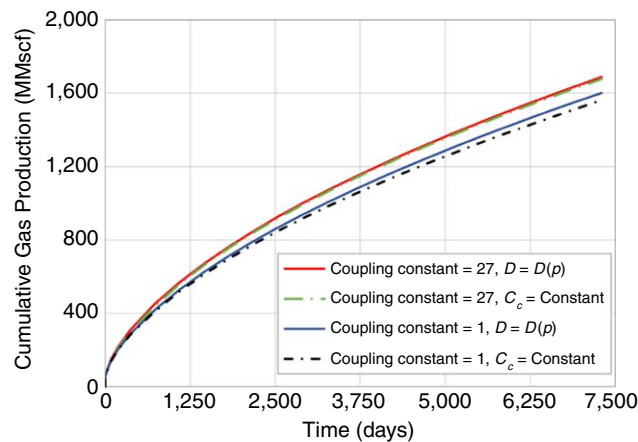


Fig. 13—The nonlinearities in the coupling factor could be more significant at lower degrees of coupling between the organic and inorganic matrices.

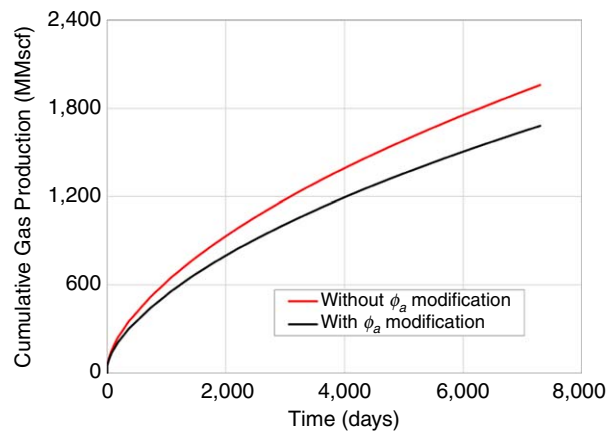


Fig. 14—Comparison of a simulation run with and without the reduction of the free-gas PV by the adsorbed-gas PV shows that the absence of this correction could lead to an overestimation of the cumulative production by approximately 17% at a flowing BHP of 2,000 psia.

with and without the reduction of the free-gas PV by the adsorbed-gas PV shows that the absence of this correction could lead to an overestimation of the cumulative production by approximately 17%. This is because the PV available for gas storage in the free state is implicitly larger by an amount that is equal to the PV taken up by the adsorbed-gas molecules. From the results shown in Fig. 14, we can infer that it is important to account for the pore spaces occupied by sorbed-gas molecules in organic-rich resource shales. The details on how this correction was implemented are discussed previously.

Contribution of Kerogen to Production in Shale-Gas Reservoirs. Given the definition of ε_{kp} as the ratio of the kerogen PV to the total PV, Fig. 15 shows the contribution of kerogen to production when the organic pores accounts for 35% of the total PV (in Fig. 15a)

and when the organic pores account for 50% of the total PV (in Fig. 15b). The black dotted lines in both Figs. 15a and 15b correspond to the cases where we essentially take out all the organic pores and model production from the inorganic pores only. The solid red lines in both Figs. 15a and 15b correspond to the cases where we model both the organic and inorganic pores at the base-case-parameter levels, and with a coupling constant (ζ) of 27. The difference between the solid red line and the dotted black line gives the contribution of the organic pores to the cumulative production. The dotted blue line in both plots shows the production performance for a system where the bulk volume occupied by kerogen is replaced by a corresponding inorganic bulk volume. The fact that the dotted blue line is higher than the solid red line in both plots indicates that for a given bulk volume, the inorganic pores tend to produce more gas than the organic pores, even though we expect more gas storage in the organic pores (because of adsorption).

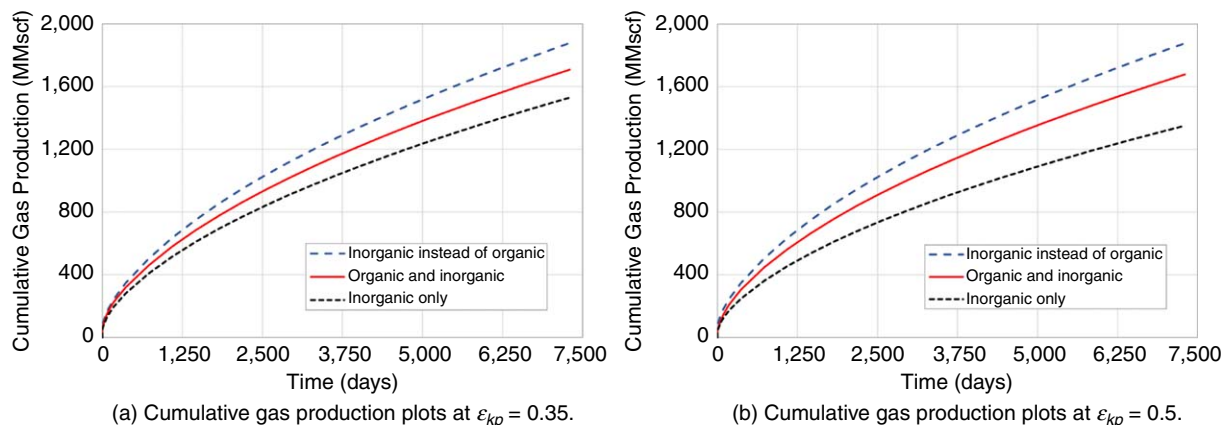


Fig. 15—Cumulative-gas-production plot shows that the dispersed kerogen in shale-gas reservoirs can contribute appreciably toward production. (a) Cumulative-gas-production plots at $\varepsilon_{kp} = 0.35$. (b) Cumulative-gas-production plots at $\varepsilon_{kp} = 0.5$.

The higher production from the dotted blue line in comparison with the solid red line could be attributed to the observation that the fractional recovery from inorganic pores is generally much larger than the corresponding fractional recovery from organic pores at typical average reservoir pressures in shale-gas reservoirs. We study the fractional recoveries associated with both free and adsorbed gases, and show that the contribution of the adsorbed gases in the organic nanopores could be curtailed by the relatively high average reservoir pressures in shales. Another possible reason for the lower production from an organic pore in comparison with an inorganic pore could be related to the curtailment of the production from the organic pores by the degree of coupling between the inorganic and the organic pores. In addition, we note that the advective transport expected in the inorganic matrix could play a major role in accelerating the rate of production from a reservoir with no organic pores, in comparison with another reservoir with some kerogen. This is because kerogen typically lacks microcracks and laminations that could contribute to accelerated advective transport. The observation that advective transport dominates diffusive transport at 100 nd or more, whereas diffusion becomes increasingly more important at less than 10 nd, suggests that we might have predominantly advective transport in the inorganic pores and predominantly diffusive transport in the organic pores. This difference in the expected transport mechanisms in the organic and inorganic pores suggests that it might be crucial to model these two continua differently, as is done in this work. A simple homogenization of the organic and inorganic continua (by use of a single-porosity simulation model, for example) without accounting for the distinct storage and transport mechanisms peculiar to each of these continua could lead to inaccurate results. This is because an assumption of advective transport in the homogenized continuum, for example, could overestimate the transport term and lead to an overestimation of the production performance by use of such a single-porosity model.

A comparison of Fig. 15a with Fig. 15b indicates that the contribution of kerogen toward cumulative production appears to be more significant when more of the pores in the total system are in the kerogen pores. This is expected given that the kerogen tends to hold more free gases in addition to the adsorbed gases at higher values of ε_{kp} . It is worth noting that high ε_{kp} -values do not automatically imply that the organic pores are continuous at the reservoir-simulation-gridblock scale. It could, however, be indicative of a lack of abundance of macropores and/or microcracks in the inorganic matrix. The generally low total-organic-carbon values (usually less than 10%) even when ε_{kp} -values are high, could indicate that kerogen is still dispersed in the inorganic matrix, which has a much-higher volume fraction than the organic matrix.

Analysis of Fractional Recovery. This subsection seeks to study the relative contribution of free and adsorbed gases to production, with the idea of explaining the results shown in Fig. 15a. The results in Fig. 16a were computed by use of the volumetric shale-gas-in-place calculations presented by Ambrose et al. (2012) and Hartman et al. (2012). These fractional recoveries were computed by subtracting the free- and sorbed-gas amounts at any pressure from the corresponding amounts at initial pressure, and dividing the result by the total (free+sorbed) gas amount at the initial conditions. In Fig. 16b, we focus on the limited range of average reservoir pressure that was observed from the numerical simulations performed. The line plots are the analytical estimates from Fig. 16a, whereas the dotted points show the corresponding fractional recoveries estimated from the numerical simulations performed. The average pressure at a given time is calculated by use of the pressure values within the radius of investigation. The results indicate that the free-gas fractional recoveries are much larger than the sorbed-gas recoveries. At the estimated average reservoir pressure of approximately 3,300 after 20 years of production, the simulation results indicated that the free-gas fractional recovery is approximately 6.3 times larger than that of the sorbed gas, whereas the analytical calculations showed it is approximately 4.7 times larger. The main difference between the analytical and numerical estimates of fractional recovery is that the numerical estimates account for the resistances to flow (and associated transient-flow effects) caused by the permeability and diffusivity of the system, whereas the analytical estimates essentially correspond to a “tank model” that does not account for the resistance and transient effects associated with the transport mechanisms in the reservoir.

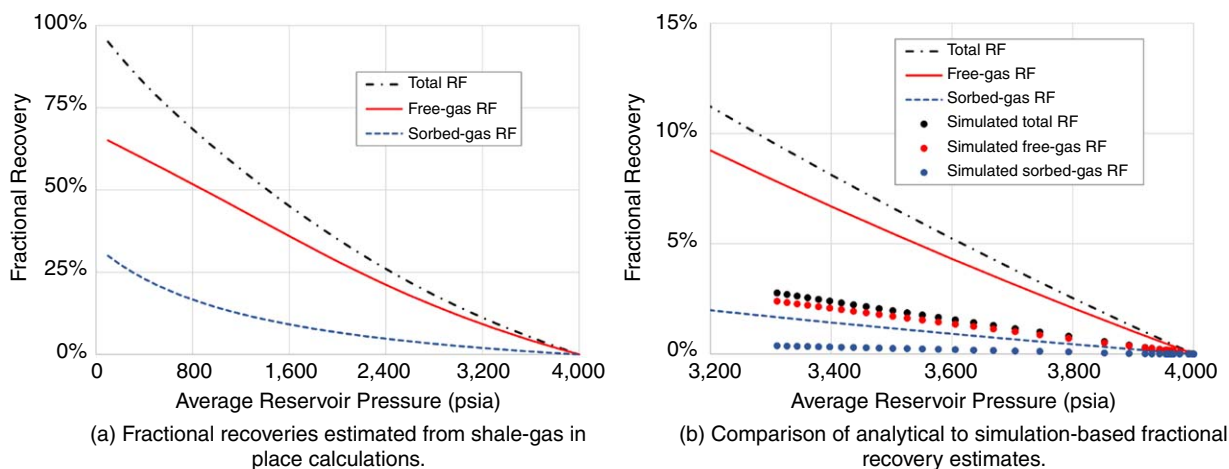


Fig. 16—The fractional recoveries indicate that the contribution of sorbed gas to total recovery could be limited at relatively high average reservoir pressures. The increase in this contribution at lower pressures could be related to the shape of the Langmuir isotherm. (a) Fractional recoveries estimated from shale-gas-in-place calculations. (b) Comparison of analytical with simulation-based fractional-recovery estimates. RF = recovery factor.

It is worth noting that free-gas molecules exist in both inorganic and organic pores. Although the free gases in the organic pores could be released at rates similar to the rate of production of free gas from the inorganic pores (if the organic and inorganic pores are fully coupled, with high ζ -values), the additional production from desorption could be limited by the low recoveries at the relatively high average pressures expected in strongly transient shale-gas reservoirs. The shape of a typical adsorption/desorption isotherm is such that the adsorbed-gas amount flattens at high pressures, but shows relatively steep declines only at very low pressures, which may be much lower than typical flowing bottomhole-pressure (BHP) values. This explains why the amount of sorbed gas desorbed at typical average reservoir pressures could be much less than the free gas produced. We note that these average reservoir pressures were estimated by use of a volume-weighted average of the cell pressures in all the gridblocks within the drainage area observed in the simulated pressure profiles.

Contribution of Diffusion at Lower Flowing BHPs. In an earlier section, we showed that the contribution of diffusion to flow in the inorganic pores could be dominated by the advective transport. In Fig. 17a, we show a slightly increased contribution of diffusion to flow at a lower flowing BHP of 500 psia, in a system with both organic and inorganic pores. The profile for the case with a constant diffusion coefficient is practically identical to the case with a pressure-dependent diffusion coefficient at a flowing BHP of 1,500 psia, whereas a slight difference is observed at a pressure of 500 psia. This can be attributed to the increased contribution of desorption to production at lower pressures, as explained previously. We expect this difference to be more significant at an even-lower pressure, but it might be unrealistic to produce a well at a much-lower pressure. The typical sharp increase in pressure (shown in Fig. 12) away from the fracture surface indicates that the increased desorption at the lower pressure of 500 psi could be limited to a small region very close to the fracture faces. Fig. 17b shows the production performance with and without organic pores at a BHP of 500 psia and at the base-case BHP of 1,500 psia. The lowest-three production profiles correspond to the cases shown in Fig. 15a, where the BHP is maintained at 1,500 psia. The production profile shows higher production at a flowing BHP of 500 psia, as expected given the increased pressure drawdown in this case.

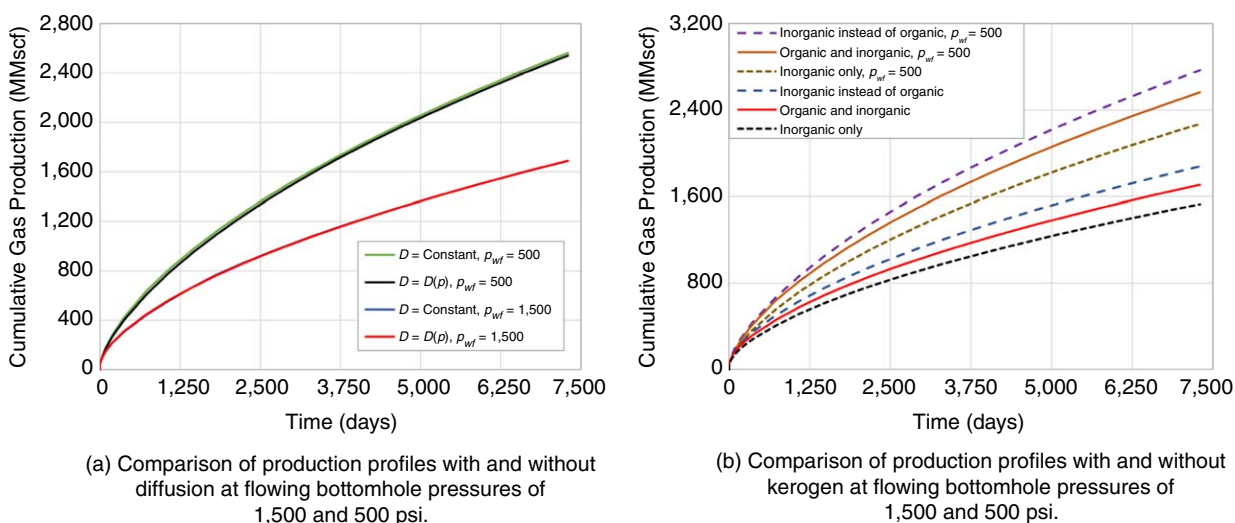


Fig. 17—The simulation results indicate that the contribution of diffusion could be more significant at lower flowing BHP values. (a) Comparison of production profiles with and without diffusion at flowing BHPs of 1,500 and 500 psi. (b) Comparison of production profiles with and without kerogen at flowing BHPs of 1,500 and 500 psi.

Analysis of Péclet Number. In this subsection, we focus on the analysis of the relative contribution of advective and diffusive transport (in the base-case simulation model, with a matrix permeability of 100 nd) by use of the Péclet number. By definition, the Péclet number is the ratio of the rate of advective transport to the rate of diffusive transport. **Fig. 18a** gives the plot of the Péclet number for CH₄ in the inorganic pores vs. the orthogonal distance away from the fracture face. Each curve on the plot corresponds to a particular snapshot in time. The relatively high values (greater than 10) of the Péclet number indicate that the rate of advective transport is much faster than the rate of diffusive transport in the inorganic pores. The gradual drop in the curves as time evolves indicates that the contribution of diffusion to transport tends to increase as the duration of the production increases. The observation that the Péclet number decreases in the direction of the fracture surface indicates that the contribution of diffusion to transport increases in the direction of the fracture surface. This contribution of diffusion is greatest in the proximity of the fracture surface, as indicated by the observation that the Péclet number is lowest right by the fracture surface. A physical explanation for the maximum contribution of diffusive transport at the fracture surfaces is related to the typical sharp drop of the gridblock pressures to the flowing BHP in the vicinity of the fracture surface. When this happens, the pressure-gradient term becomes small in magnitude, leading to a reduction in the advective transport and a consequent decrease in the Péclet number. A similar trend is observed in the Péclet number for ethane (C₂H₆), which is given in Fig. 18b. Comparing Fig. 18b with Fig. 18a, we observe that the Péclet numbers for C₂H₆ are generally greater than the Péclet numbers for CH₄. This is expected because CH₄ is lighter than C₂H₆, and its rate of diffusion is generally faster than that of C₂H₆ under the same conditions.

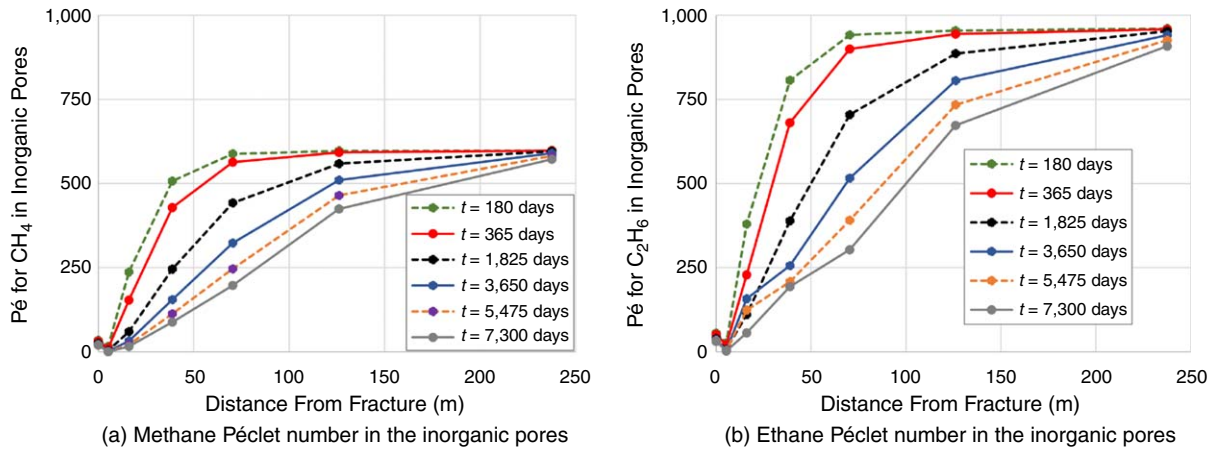


Fig. 18—The Péclet number for CH₄ and C₂H₆ in the inorganic pores indicates that advective transport could be the dominant transport mechanism in the reservoir. (a) CH₄ Péclet number in the inorganic pores. (b) C₂H₆ Péclet number in the inorganic pores.

In **Fig. 19**, we introduce the pseudo-Péclet number, which is simply the ratio of the rate of advective transport in the inorganic pores to the rate at which gas is released from the organic pores into the inorganic pores. The results indicate that the rate of advective transport in the inorganic pores is faster than the rate at which gas is released from the organic pores into the inorganic pores. These results are consistent with the results shown in the subsection Analysis of Fractional Recovery, where we show that the fractional recovery from inorganic pores is generally larger than the fractional recovery from the organic pores. This is because of the higher resistance to flow in the organic pores, the dispersed nature of these organic pores, as well as the curtailed desorption of gas at relatively high pressures, as discussed in that subsection. Furthermore, comparing Fig. 19a with Fig. 19b, we note that the pseudo-Péclet numbers for CH₄ are generally lower than those for C₂H₆ because the rate of diffusion of CH₄ is generally faster than that of C₂H₆ under the same conditions.

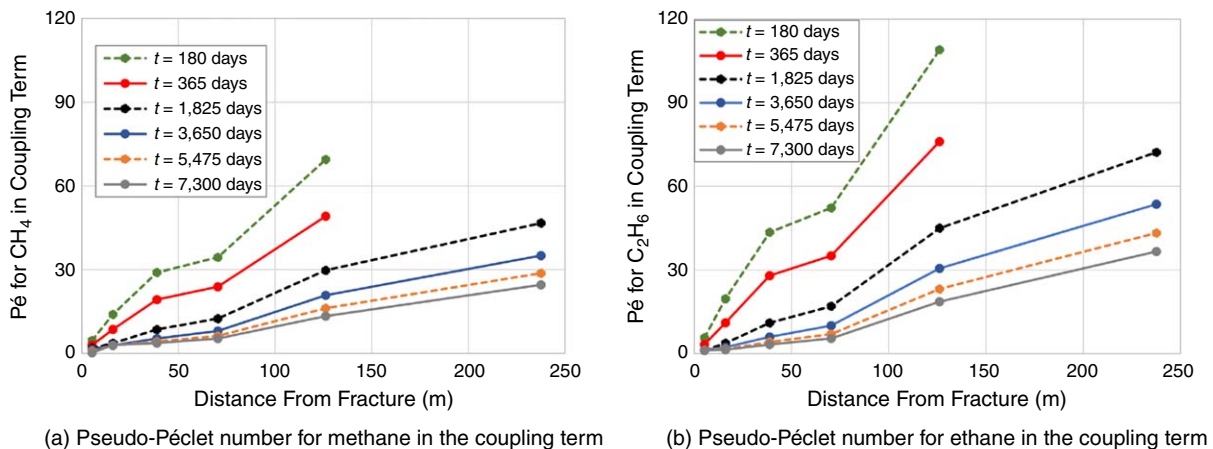


Fig. 19—The pseudo-Péclet numbers for CH₄ and C₂H₆ indicate that the rate of advective transport in the inorganic pores is much faster than the rate at which gas is released from the organic pores into the inorganic pores. (a) Pseudo-Péclet number for CH₄ in the coupling term. (b) Pseudo-Péclet number for C₂H₆ in the coupling term.

Effect of the Pressure Dependence of Permeability and Diffusion Coefficient on Production in Shale-Gas Reservoirs. Fig. 20 gives the cumulative production plot for the cases run to study how gas production is affected by the pressure dependence of the diffusion coefficient and the stress dependence of permeability.

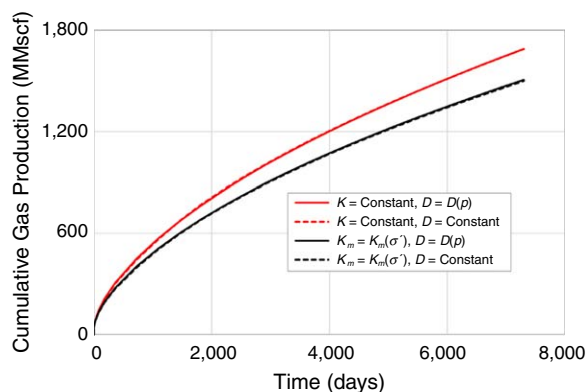


Fig. 20—Simulation results indicate that the contribution of the pressure dependence of diffusion is negligible, whereas the contribution of the stress dependence of matrix permeability could be significant at an initial reservoir permeability of 100 nd.

The dotted lines correspond to the cases where the diffusion coefficients are kept constant, whereas the solid lines correspond to the cases where the diffusion coefficients are inversely proportional to pressure. As explained in the results on the study of the effect of diffusion, the cases with and without the pressure dependence of the diffusion coefficient are indistinguishable because diffusive transport appears to be insignificant at a matrix permeability of 100 nd. The inverse proportionality of the Maxwell-Stefan diffusion coefficients comes from the kinetic theory of gases, which was used to obtain the binary-diffusion coefficients.

In Fig. 20, the red lines correspond to the cases where we assume that the matrix permeability is constant, whereas the black lines are representative of the cases where we model the stress dependence of the matrix permeability by use of the Gangi (1978) model. The difference in production between the red and the black lines could be attributed to the reduction in matrix permeability in response to pressure depletion during production. Given that the results presented in this paper are dependent on infinite-conductivity hydraulic fractures, we neglect the possible changes in fracture permeability and aperture during production.

Conclusions

This work presents a multiple-continuum model for multicomponent gas transport in organic-rich source rocks. The model presented captures the dispersed nature of kerogen observed in SEM images, and the consequent series coupling between the organic and inorganic pores. In addition, we model the molecular diffusion in organic and inorganic shale pores by use of the multicomponent Maxwell-Stefan diffusion formulation. This allows us to account for the pressure and composition dependence of molecular diffusion. A simplified version of the simulator built as part of this work was validated against Eclipse 300 for a multicomponent system without organic pores.

The numerical studies performed in this work showed that advective transport dominated diffusive transport in the inorganic pores of the representative Barnett shale-gas reservoir simulated. However, at lower values of permeability (10 nd and lower), the contribution of diffusion to the total transport becomes increasingly significant. This coupled with the expected lack of cracks and large macropores in kerogen suggests that advective transport could be negligible in organic pores, whereas the predominant transport mechanism could be diffusive (free-gas and adsorbed-gas diffusion). Considering that most commercially viable unconventional resources are expected to have more than 10 nd of matrix permeability, the contribution of molecular diffusion to the transport in these organic-rich source rocks is expected to be negligible. This work argues that it could be crucial to model the organic and inorganic continua separately, given the expected physical differences in the transport mechanisms that prevail in these two continua, and the dispersed nature of kerogen.

The results of this work showed the importance of correcting the free-gas PV for the PV occupied by the gas molecules adsorbed on the organic-pore walls. The comparison of a shale-gas simulation model with a similar model with all the organic pores replaced by inorganic pores indicated that although organic pores could contribute significantly toward the total storage in resource shales, the contribution of these organic pores to the cumulative gas production (during the typical production life of these unconventional resources) could be severely curtailed by the generally lower recoveries associated with desorption at relatively high average reservoir pressures, as well as the degree of coupling between the organic and inorganic pores. This further supports the argument that the microscale nature of resource shales is important and should not be ignored because this could result in an overestimation of the contribution of the discontinuous organic matter. The sensitivity studies on the degree of coupling between the organic and inorganic pores indicate that the contribution of the organic pores to total production peaks at a particular value of the coupling constant. The study of the effect of the stress dependence of matrix permeability showed that this effect could be significant in resource shales.

Nomenclature

B = drag matrix

c = total concentration or total molar density, mol/m³

c_G = concentration or molar density of the gas phase, mol/m³

c_i = concentration or molar density of component i , mol/m³

c_L = Langmuir concentration, mol/m³

c_μ = adsorbed-gas concentration in kerogen in mole per grain volume, mol/m³

$c_{\mu s}$ = maximum monolayer gas adsorption on the internal kerogen solid surfaces (in mole per grain volume, mol/m³)

C_c = coupling coefficient
 \mathbf{D} = matrix of diffusion coefficients in inorganic pores, m^2/s
 \mathbf{D}_k = matrix of diffusion coefficients in organic pores, m^2/s
 $D(p)$ = pressure-dependent diffusion coefficient
 \mathbf{D}_s = matrix of surface diffusion coefficients in kerogen, m^2/s
 J_i = relative (molar) flux of component i
 k = matrix permeability, m^2
 l_m = shape factor
 p = pressure, Pa
 p_{wf} = flowing BHP
 \mathbf{v} = total Darcy velocity of the bulk phase, m/s
 \mathbf{y} = vector of mole fractions of component i in the gas phase
 y_i = mole fraction of component i in the gas phase
 \mathbf{z} = vector of overall mole fractions
 z_i = overall mole fraction of component i
 Γ = matrix of thermodynamic factor
 ε_{kp} = kerogen PV per total matrix PV
 ε_{ks} = total organic content in terms of organic grain volume per total grain volume
 μ = viscosity, Pa·s
 τ = tortuosity
 ϕ = porosity

Subscripts

f = fracture
 g = gas
 k = kerogen
 k_p = kerogen pore
 k_s = kerogen matrix/solid
 m = matrix
 n_c = number of components

Superscripts

i = arbitrary composition index
 I = inorganic
 O = organic
 PSS = pseudosteady state
 T = transient

References

- Akkutlu, I. Y. and Fathi, E. 2012. Multiscale Gas Transport in Shales With Local Kerogen Heterogeneities. *SPE J.* **17** (4): 1002–1011. SPE-146422-PA. <https://doi.org/10.2118/146422-PA>.
- Akkutlu, I. Y., Efendiev, Y., and Vasilyeva, M. 2016. Multiscale Model Reduction for Shale Gas Transport in Fractured Media. *Computat. Geosci.* **20** (5): 953–973. <https://doi.org/10.1007/s10596-016-9571-6>.
- Ambrose, R. J. 2011. *Micro-Structure of Gas Shales and Its Effects on Gas Storage and Production Performance*. PhD dissertation, University of Oklahoma, Norman, Oklahoma.
- Ambrose, R. J., Hartman, R. C., Diaz-Campos, M. et al. 2012. Shale Gas-in-Place Calculations Part I: New Pore-Scale Considerations. *SPE J.* **17** (1): 219–229. SPE-131772-PA. <https://doi.org/10.2118/131772-PA>.
- Azom, P. N. and Javadpour, F. 2012. Dual-Continuum Modeling of Shale and Tight Gas Reservoirs. Presented at the SPE Annual Technical Conference and Exhibition, San Antonio, Texas, 8–10 October. SPE-159584-MS. <https://doi.org/10.2118/159584-MS>.
- Bruggeman, V. D. 1935. Berechnung verschiedener physikalischer konstanten von heterogenen substanzen. i. dielektrizitätskonstanten und leitfähigkeiten der mischkörper aus isotropen substanzen (in German). *Ann Phys* **416**: 636–664.
- Cao, H. 2002. *Development of Techniques for General Purpose Simulators*. PhD dissertation, Stanford University, Stanford, California (June 2002).
- Chen, Z., Huan, G., and Ma, Y. 2006. *Computational Methods for Multiphase Flows in Porous Media*. Philadelphia, Pennsylvania: Society for Industrial and Applied Mathematics.
- Cordazzo, J., Hurtado, F. S. V., Maliska, C. R. et al. 2003. Numerical Techniques for Solving Partial Differential Equations in Heterogeneous Media. Oral presentation given at the XXIV Iberian Latin-American Congress on Computational Methods in Engineering, Ouro Preto, Brazil, 29–31 October.
- Cordazzo, J., Maliska, C., da Silva, A. F. C. et al. 2005. An Element Based Conservative Scheme Using Unstructured Grids For Reservoir Simulation. Presented at the 18th World Petroleum Congress, Johannesburg, South Africa, 25–29 September. WPC-18-1029.
- Danner, R. P. and Daubert, T. E. 1983. *Manual for Predicting Chemical Process Design Data: Data Prediction Manual*. New York City: American Institute of Chemical Engineers.
- Efendiev, Y., Lee, S., Li, G. et al. 2015. Hierarchical Multiscale Modeling for Flows in Fractured Media Using Generalized Multiscale Finite Element Method. *GEM-Int. J. Geomath.* **6** (2): 141–162. <https://doi.org/10.1007/s13137-015-0075-7>.
- Eymard, R. and Sonier, F. 1994. Mathematical and Numerical Properties of Control-Volume Finite-Element Scheme for Reservoir Simulation. *SPE Res Eng* **9** (4): 283–289. SPE-25267-PA. <https://doi.org/10.2118/25267-PA>.
- Fathi, E. and Akkutlu, I. Y. 2014. Multi-Component Gas Transport and Adsorption Effects During CO₂ Injection and Enhanced Shale Gas Recovery. *Int. J. Coal Geol.* **123** (1 March): 52–61. <https://doi.org/10.1016/j.coal.2013.07.021>.
- Forsyth, P. A. 1990. A Control-Volume, Finite-Element Method for Local Mesh Refinement in Thermal Reservoir Simulation. *SPE Res Eng* **5** (4): 561–566. SPE-18415-PA. <https://doi.org/10.2118/18415-PA>.

- Freeman, C., Moridis, G. J., Michael, G. E. et al. 2012. Measurement, Modeling, and Diagnostics of Flowing Gas Composition Changes in Shale Gas Wells. Presented at the SPE Latin America and Caribbean Petroleum Engineering Conference, Mexico City, 16–18 April. SPE-153391-MS. <https://doi.org/10.2118/153391-MS>.
- Fuller, E. N., Ensley, K., and Giddings, J. C. 1969. Diffusion of Halogenated Hydrocarbons in Helium. The Effect of Structure on Collision Cross Sections. *J. Phys. Chem.* **73** (11): 3679–3685. <https://doi.org/10.1021/j100845a020>.
- Fuller, E. N., Schettler, P. D., and Calvin, J. 1966. Giddings. New Method for Prediction of Binary Gas-Phase Diffusion Coefficients. *Ind. Eng. Chem.* **58** (5): 18–27. <https://doi.org/10.1021/ie50677a007>.
- Fung, L. S. K., Hiebert, A. D., and Nghiem, L. X. 1992. Reservoir Simulation With a Control-Volume Finite-Element Method. *SPE Res Eng* **7** (3): 349–357. SPE-21224-PA. <https://doi.org/10.2118/21224-PA>.
- Gangi, A. F. 1978. Variation of Whole and Fractured Porous Rock Permeability With Confining Pressure. *Int. J. Rock Mech. Min.* **15** (5): 249–257. [https://doi.org/10.1016/0148-9062\(78\)90957-9](https://doi.org/10.1016/0148-9062(78)90957-9).
- Geuzaine, C. and Remacle, J. F. 2009. Gmsh: A 3-D Finite Element Mesh Generator With Built-In Pre- and Post-Processing Facilities. *Int. J. Numer. Meth. Eng.* **79** (11): 1309–1331. <https://doi.org/10.1002/nme.2579>.
- Hartman, R. C., Ambrose, R. J., Akkutlu, I. Y. et al. 2012. Shale Gas-in-Place Calculations Part II - Multicomponent Gas Adsorption Effects. Presented at the North American Unconventional Gas Conference and Exhibition, The Woodlands, Texas, 14–16 June. SPE-144097-MS. <https://doi.org/10.2118/144097-MS>.
- Heinemann, Z. E. and Mittermeir, G. M. 2012. Derivation of the Kazemi–Gilman–Elsharkawy Generalized Dual Porosity Shape Factor. *Transport Porous Med.* **91** (1): 123–132. <https://doi.org/10.1007/s11242-011-9836-4>.
- Hoteit, H. 2011. Proper Modeling of Diffusion in Fractured Reservoirs. Presented at the SPE Reservoir Simulation Symposium, The Woodlands, Texas, 21–23 February. SPE-141937-MS. <https://doi.org/10.2118/141937-MS>.
- Hoteit, H. and Firoozabadi, A. 2009. Numerical Modeling of Diffusion in Fractured Media for Gas-Injection and -Recycling Schemes. *SPE J.* **14** (2): 323–337. SPE-103292-PA. <https://doi.org/10.2118/103292-PA>.
- Hu, Q.-H. and Ewing, R. P. 2014. Integrated Experimental and Modeling Approaches to Studying the Fracture-Matrix Interactions in Gas Recovery from Barnett Shale. Research Partnership to Secure Energy for America Project Fact Sheet, Project No. 09122-12.
- Hu, Q.-H., Liu, X.-G., Gao, Z.-Y. et al. 2015. Pore Structure and Tracer Migration Behavior of Typical American and Chinese Shales. *Petrol. Sci.* **12** (4): 651–663. <https://doi.org/10.1007/s12182-015-0051-8>.
- Hurtado, F. S. V., Maliska, C. R., da Silva, A. F. C. et al. 2007. A Quadrilateral Element-Based Finite-Volume Formulation for the Simulation of Complex Reservoirs. Presented at the Latin American & Caribbean Petroleum Engineering Conference, Buenos Aires, 15–18 April. SPE-107444-MS. <https://doi.org/10.2118/107444-MS>.
- Kang, S. M., Fathi, E., Ambrose, R. J. et al. 2011. Carbon Dioxide Storage Capacity of Organic-Rich Shales. *SPE J.* **16** (4): 842–855. SPE-134583-PA. <https://doi.org/10.2118/134583-PA>.
- Kazemi, H., Gilman, J. R., and Elsharkawy, A. M. 1992. Analytical and Numerical Solution of Oil Recovery From Fractured Reservoirs With Empirical Transfer Functions. *SPE Res Eng* **7** (2): 219–227. SPE-19849-PA. <https://doi.org/10.2118/19849-PA>.
- Kim, J.-G. and Deo, M. D. 2000. Finite Element, Discrete-Fracture Model for Multiphase Flow in Porous Media. *AICHE J.* **46** (6): 1120–1130. <https://doi.org/10.1002/aic.690460604>.
- Lee, A. L., Gonzalez, M. H., and Eakin, B. E. 1966. The Viscosity of Natural Gases. *J. Pet Technol* **18** (8): 997–1000. SPE-1340-PA. <https://doi.org/10.2118/1340-PA>.
- Lemonnier, P. A. 1979. Improvement Of Reservoir Simulation By A Triangular Discontinuous Finite Element Method. Presented at the SPE Annual Technical Conference and Exhibition, Las Vegas, 23–26 September. SPE-8249-MS. <https://doi.org/10.2118/8249-MS>.
- Li, L. and Lee, S. H. 2008. Efficient Field-Scale Simulation of Black Oil in a Naturally Fractured Reservoir Through Discrete Fracture Networks and Homogenized Media. *SPE Res Eval & Eng* **11** (4): 750–758. SPE-103901-PA. <https://doi.org/10.2118/103901-PA>.
- Loucks, R. G., Reed, R. M., Ruppel, S. C. et al. 2009. Morphology, Genesis, and Distribution of Nanometer-Scale Pores in Siliceous Mudstones of the Mississippian Barnett Shale. *J. Sediment. Res.* **79** (12): 848–861. <https://doi.org/10.2110/jsr.2009.092>.
- Loucks, R. G., Reed, R. M., Ruppel, S. C. et al. 2012. Spectrum of Pore Types and Networks in Mudrocks and a Descriptive Classification for Matrix-Related Mudrock Pores. *AAPG Bull.* **96** (6): 1071–1098. <https://doi.org/10.1306/08171111061>.
- Lu, H., Di Donato, G., and Blunt, M. J. 2008. General Transfer Functions for Multiphase Flow in Fractured Reservoirs. *SPE J.* **13** (3): 289–297. SPE-102542-PA. <https://doi.org/10.2118/102542-PA>.
- Monteagudo, J. E. P. and Firoozabadi, A. 2004. Control-Volume Method for Numerical Simulation of Two-Phase Immiscible Flow in Two- and Three-Dimensional Discrete-Fractured Media. *Water Resour. Res.* **40** (7): W07405. <https://doi.org/10.1029/2003WR002996>.
- Noorishad, J. and Mehran, M. 1982. An Upstream Finite Element Method for Solution of Transient Transport Equation in Fractured Porous Media. *Water Resour. Res.* **18** (3): 588–596. <https://doi.org/10.1029/WR018i003p00588>.
- Olorode, O., Freeman, C. M., Moridis, G. et al. 2013. High-Resolution Numerical Modeling of Complex and Irregular Fracture Patterns in Shale-Gas Reservoirs and Tight Gas Reservoirs. *SPE Res Eval & Eng* **16** (4): 443–455. SPE-152482-PA. <https://doi.org/10.2118/152482-PA>.
- Orangi, A., Nagarajan, N. R., Honarpour, M. M. et al. 2011. Unconventional Shale Oil and Gas-Condensate Reservoir Production, Impact of Rock, Fluid, and Hydraulic Fractures. Presented at the SPE Hydraulic Fracturing Technology Conference, The Woodlands, Texas, 24–26 January. SPE-140536-MS. <https://doi.org/10.2118/140536-MS>.
- Peng, D.-Y. and Robinson, D. B. 1976. A New Two-Constant Equation of State. *Ind. Eng. Chem. Fundamen.* **15** (1): 59–64. <https://doi.org/10.1021/i160057a011>.
- Reid, R. C., Prausnitz, J. M., and Poling, B. E. 1987. *The Properties of Gases and Liquids*, fourth edition. New York City: McGraw-Hill.
- Revil, A., Woodruff, W. F., Torres-Verdín, C. et al. 2013. Complex Conductivity Tensor of Anisotropic Hydrocarbon-Bearing Shales and Mudrocks. *Geophysics* **78** (6): D403–D418. <https://doi.org/10.1190/geo2013-0100.1>.
- Sun, H., Chawathe, A., Hoteit, H. et al. 2015. Understanding Shale Gas Flow Behavior Using Numerical Simulation. *SPE J.* **20** (1): 142–154. SPE-167753-PA. <https://doi.org/10.2118/167753-PA>.
- Syihab, Z. 2009. *Simulation on Discrete Fracture Network Using Flexible Voronoi Gridding*. PhD dissertation, Texas A&M University, College Station, Texas.
- Taylor, R. and Krishna, R. 1993. *Multicomponent Mass Transfer*. New York City: John Wiley and Sons.
- Voller, V. R. 2009. *Basic Control Volume Finite Element Methods for Fluids and Solids*. Hackensack, New Jersey: World Scientific Publishing Co. Pte. Ltd.
- Walas, S. M. 1985. *Phase Equilibria in Chemical Engineering*. Stoneham, Massachusetts: Butterworth Publishers.
- Warren, J. E. and Root, P. J. 1963. The Behavior of Naturally Fractured Reservoirs. *SPE J.* **3** (3): 245–255. SPE-426-PA. <https://doi.org/10.2118/426-PA>.
- Wasaki, A. and Akkutlu, I. Y. 2015. Permeability of Organic-Rich Shale. *SPE J.* **20** (6): 1384–1396. SPE-170830-PA. <https://doi.org/10.2118/170830-PA>.
- Xiong, Y., Winterfeld, P., Wang, C. et al. 2015. Effect of Large Capillary Pressure on Fluid Flow and Transport in Stress-sensitive Tight Oil Reservoirs. Presented at the SPE Annual Technical Conference and Exhibition, Houston, 28–30 September. SPE-175074-MS. <https://doi.org/10.2118/175074-MS>.

Yi, J., Akkutlu, I. Y., and Deutsch, C. V. 2008. Gas Transport in Bidisperse Coal Particles: Investigation for an Effective Diffusion Coefficient in Coalbeds. *J Can Pet Technol* 47 (10): 20–26. PETSOC-08-10-20. <https://doi.org/10.2118/08-10-20>.

Zhang, M., Yao, J., Sun, H. et al. 2015. Triple-Continuum Modeling of Shale Gas Reservoirs Considering the Effect of Kerogen. *J. Nat. Gas Sci. Eng.* 24 (May): 252–263. <https://doi.org/10.1016/j.jngse.2015.03.032>.

Zimmerman, R. W., Chen, G., Hadgu, T. et al. 1993. A Numerical Dual-Porosity Model with Semianalytical Treatment of Fracture/Matrix Flow. *Water Resour. Res.* 29 (7): 2127–2137. <https://doi.org/10.1029/93WR00749>.

Appendix A—Estimation of Kerogen Bulk Volume V_b^k

Appendix A shows the derivation of an expression for the kerogen bulk volume in terms of input parameters ε_{ks} , ε_{kp} , and ϕ and bulk volume V_b .

By definition,

$$\varepsilon_{ks} = \frac{GV_k}{GV}, \dots \dots \dots (A-1)$$

where GV is grain volume. This implies that

$$GV_k = \varepsilon_{ks}GV. \dots \dots \dots (A-2)$$

Similarly, from the definition of ε_{kp} as the ratio of the kerogen PV to the total PV, we obtain

$$PV_k = \varepsilon_{kp}PV. \dots \dots \dots (A-3)$$

By volume balance,

$$V_b^k = PV_k + GV_k. \dots \dots \dots (A-4)$$

Substituting Eqs. A-2 and A-3 into Eq. A-4 yields

$$V_b^k = \varepsilon_{kp}PV + \varepsilon_{ks}GV. \dots \dots \dots (A-5)$$

Because porosity is defined as the ratio of PV to bulk volume, we can write PV as

$$PV = \phi V_b. \dots \dots \dots (A-6)$$

Similarly, we can express GV as

$$GV = (1 - \phi)V_b. \dots \dots \dots (A-7)$$

Substituting Eqs. A-6 and A-7 into Eq. A-5, we obtain

$$V_b^k = \varepsilon_{kp}\phi V_b + \varepsilon_{ks}(1 - \phi)V_b. \dots \dots \dots (A-8)$$

Appendix B—Computations of Geometric Factor \mathcal{G}_A

We have already shown how to compute the geometric factor for a sphere with radius r and a cube with sides x . Here, we proceed to show the computation of some rectangular geometries with sides that are functions of x . The idea is to show the effect of these aspect ratios on the estimated geometrical factors that go into the computation of the shape factor. **Fig. B-1** shows the cube, the geometric factor of which was determined in the paper, together with two other cuboids with different aspect ratios.

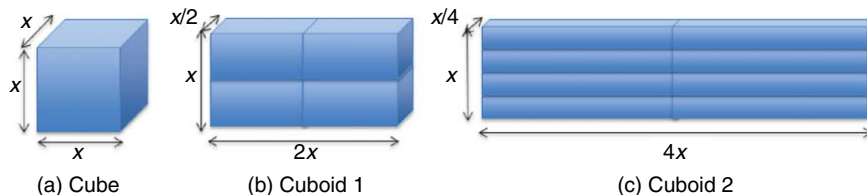


Fig. B-1—Illustration of the effect of aspect ratios on geometric factors.

Following the procedure explained previously, the geometric factor \mathcal{G}_A for Cuboid 1 is 21, whereas that for Cuboid 2 is 68.25. This shows that the geometric factor increases significantly as the kerogen geometry gets flatter and longer. The comparison of the geometric factor of the cube with that of the sphere (given previously) indicates that the shape factor for a flat surface is less than that for a convex surface. We also expect that the shape factor for a concave surface will be further less than that for a flat surface.

In comparison with the shape factors for conventional dual-porosity models for matrix and fractures, we expect the shape factors for kerogen in shales to be much larger because of the rather dispersed nature in which kerogen is deposited in shales, as seen in SEM

images. The dispersed kerogen matrix is expected to give larger shape factors than the rather large and blocky matrices that are typically seen in the illustrations of the Warren and Root (1963) model.

Olufemi Olorode is a PhD degree candidate in the Petroleum Engineering Department at Texas A&M University. He has 4 years of experience in the oil and gas industry as a petroleum engineer at Afren Resources. Olorode specializes in the areas of reservoir simulation, history matching, and production forecasting. He has authored or coauthored several publications in the area of shale-gas numerical modeling. Olorode serves as a technical reviewer for *SPE Journal* and *Journal of Petroleum Science and Engineering*. He holds a master's degree in petroleum engineering from Texas A&M University.

I. Yucel Akkutlu is the Flotek Industries Incorporated Career Development Professor in the Harold Vance Department of Petroleum Engineering at Texas A&M University. He is a chemical engineer whose main research interests are fluid flow, transport, and reactions in porous media. Akkutlu served as the executive editor of *SPE Journal* from 2012 to 2015 and was an SPE Distinguished Lecturer during the 2014–2015 season. He received the 2016 Texas A&M University Distinguished Achievement Award, the 2015 AIME Rossiter W. Raymond Memorial Award, the 2015 Texas A&M University College of Engineering William Keeler Faculty Fellow Award, and the 2015 Texas A&M University Petroleum Engineering Department Karen and Larry Cress Excellence in Teaching Faculty Award. Akkutlu holds a PhD degree in petroleum engineering from the University of Southern California.

Yalchin Efendiev is a professor in the Mathematics Department of Texas A&M University. He joined Texas A&M University in 2001. Efendiev's research interests are in multiscale modeling and upscaling. He holds a PhD degree in applied mathematics from California Institute of Technology.